

---

# Variable cosmological parameters and their effects on the 21-cm Cosmic Dawn signal

---

*Author:*Kyle Wong  
(kyhw2)*Supervisors:*Prof. Anastasia Fialkov  
Jiten Dhandha

## Abstract

21-cm cosmology is a promising probe of early Universe evolution, particularly in the cosmic eras known as the Dark Ages, Cosmic Dawn, and Epoch of Reionization. Processes which occur during these periods are sensitive to the underlying cosmological parameters – as such, the 21-cm signal provides insight into their measurement. While 21-cm simulations such as 21cmSPACE focus predominantly on modelling the astrophysical processes prevalent during the early Universe, the ability to vary the underlying cosmology will enable the study of the propagation of cosmological parameters onto the 21-cm signal. This report details a step in this direction: the implementation of variable cosmological parameters onto the generation of initial conditions (the initial mass over-density field  $\delta_m$  and relative velocity field between baryons and cold dark matter  $v_{bc}$ ) in 21cmSPACE, and the effects of changing some of these parameters is discussed. In particular, varying the mass density  $\Omega_m$ , the baryon density  $\Omega_b$ , and the Hubble constant  $h$  are shown to significantly affect the timing of cosmological eras, resulting in distortions of the 21-cm global signal and the 21-cm power spectrum.

# CONTENTS

I. Introduction	3
A. 21-cm cosmology	3
II. Theoretical background	4
A. 21-cm signal fundamentals	4
B. Cosmic history	5
1. Dark Ages ( $z \sim 1100 - 30$ )	5
2. Cosmic Dawn ( $z \sim 30 - 15$ )	5
3. Epoch of Reionization ( $z \sim 15 - 6$ )	6
C. 21-cm observables	7
D. Initial conditions	8
1. Mass over-density fields	8
2. Streaming velocity effect	9
III. 21cmSPACE	10
A. Design principles	10
B. Code execution	11
C. Project motivation and impact	12
IV. Methodology	13
A. Initial conditions generation	13
B. Consistency checks	16
V. Results and discussion	19
A. Simulation suite	19
B. Varying $\Omega_m$	22
C. Varying $\Omega_b$	24
D. Varying $h$	26
VI. Conclusions and future work	28
A. Conclusions	28
B. Future work	28
Acknowledgments	29
References	29

## I. INTRODUCTION

### A. 21-cm cosmology

Understanding the formation and evolution of cosmic structure remains one of the central goals of modern cosmology. While observations of the cosmic microwave background (CMB) and large-scale structure surveys have provided invaluable insights into the early and late-time Universe, there exists a significant observational gap between the release of the CMB ( $\sim 380,000$  years after the Big Bang) and the emergence of the first luminous structures several hundred million years later. This intermediate period, encompassing the so-called Dark Ages, Cosmic Dawn, and the Epoch of Reionization (EoR), holds crucial information about the Universe’s thermal and ionization history, the formation of the first stars and galaxies, and the onset of feedback processes.

21-cm cosmology offers a unique and powerful tool to probe this otherwise inaccessible era. The signal arises from the hyperfine transition of neutral hydrogen (HI), which occurs when the relative spin orientation of the proton and electron flips between parallel and antiparallel, emitting or absorbing a photon with a rest-frame wavelength of 21 centimetres. Because neutral hydrogen was the most abundant element in the early Universe, the 21-cm line provides a pervasive and potentially highly informative tracer of matter distribution over cosmic time.

As the Universe expands, the 21-cm signal is redshifted, allowing observations at different frequencies corresponding to different epochs. By mapping the sky across frequency channels, it is, in principle, possible to construct a three-dimensional tomographic view of the intergalactic medium (IGM). This makes the 21-cm line a particularly sensitive probe for the thermal history of the IGM, the timing and topology of reionization, the formation of the first stars and black holes, and potentially, physics beyond the standard cosmological model, such as dark matter interactions or exotic energy injection.

Detecting this signal presents substantial technical challenges. The cosmological 21-cm signal is typically five orders of magnitude fainter than galactic and extragalactic foregrounds, including synchrotron emission from our Galaxy. Additionally, instrumental systematics, ionospheric effects, and radio frequency interference (RFI) must be mitigated with extreme precision.

Despite these obstacles, a growing number of dedicated low-frequency radio interferometers — such as LOFAR (van Haarlem et al. 2013), MWA (Beardsley et al. 2019), HERA (DeBoer et al. 2017), and the upcoming Square Kilometre Array (SKA) Dewdney et al. (2009) — are designed to detect and characterize the 21-cm signal from the early Universe. These instruments aim to measure the power spectrum of 21-cm fluctuations, and eventually, perform direct imaging of the neutral IGM.

The addition of 21-cm cosmology to the field of observational astronomy is an exciting prospect, potentially offering a detailed timeline of the Universe’s first billion years and enabling precision tests of fundamental physics in a previously uncharted epoch.

## II. THEORETICAL BACKGROUND

### A. 21-cm signal fundamentals

The 21-cm signal is the result of the hyperfine transition of atomic hydrogen, which, as both the most abundant and most basic element, is comprised of a single electron combined with a single proton. Due to the slight energy discrepancy between the spin-aligned state of this electron-proton pair and the spin-antialigned state, during this transition, atomic hydrogen can either emit or absorb a photon of wavelength 21 centimeters. The spin temperature  $T_s$  is useful for studying the 21-cm emission line, and is given by (Purcell & Field 1956; Scott & Rees 1990)

$$\frac{n_1}{n_0} = 3 \exp\left(-\frac{h \nu_{21}}{k_b T_s}\right) \quad (1)$$

where  $n_1/n_0$  is the number of hydrogen atoms in the excited hyperfine (aligned) state over the number of hydrogen atoms in the ground hyperfine (anti-aligned) state,  $h$  is Planck's constant,  $k_b$  is Boltzmann's constant, and  $\nu_{21} \approx 1420.406$  MHz is the frequency of the 21-cm emission line in the rest frame.

It is important to note that the spin temperature is not directly observed; rather, it is the difference between the CMB temperature  $T_{\text{CMB}}$  and the 21-cm spin temperature which is measured. Areas in which the 21-cm spin temperature is higher than the CMB temperature result in excess emission compared to what is expected from CMB emissions; on the contrary, when  $T_s < T_{\text{CMB}}$ , a photon deficit is measured instead. This difference between temperatures is defined as the *brightness temperature*  $T_{21}$ , which is written in terms of  $T_s$  as (Furlanetto et al. 2006)

$$T_{21}(\hat{\mathbf{r}}, \nu) = [1 - \exp(-\tau_{21}(\hat{\mathbf{r}}, z))] \frac{T_s(\hat{\mathbf{r}}, z) - T_{\text{CMB}}(z)}{1 + z} \quad (2)$$

where  $\hat{\mathbf{r}}$  is a radial unit vector from the observer in the direction of observation, the doppler-shifted frequency of the observed signal  $\nu$  is given by

$$1 + z = \frac{\nu_{21}}{\nu} \quad (3)$$

and  $\tau_{21}$  is the 21-cm optical depth (i.e., how much 21-cm light is absorbed or scattered) of the interstellar medium, defined as

$$\tau_{21}(\hat{\mathbf{r}}, z) = \frac{3\hbar c^3 A_{10}}{16k_b \nu_{21}^2} \frac{x_{\text{HI}} n_{\text{H}}}{(1+z)(dv_{\parallel}/dr_{\parallel}) T_s} \quad (4)$$

with  $v_{\parallel}$  the proper velocity along the line of sight  $r_{\parallel}$ ,  $x_{\text{HI}}$  and  $n_{\text{H}}$  are the fraction and number density of neutral hydrogen atoms respectively,  $\hbar$  is Planck's constant divided by  $2\pi$ ,  $c$  is the speed of light, and  $A_{10} = 2.85 \times 10^{-15} \text{s}^{-1}$  is the spontaneous emission coefficient of the hyperfine transition, quantifying the probability that an atom in the aligned state will spontaneously decay into the anti-aligned state.

In the linear limit where the 21-cm line is optically thin ( $\tau_{21} \ll 1$ ), which is true at all regions of interest (Lewis & Challinor 2007), the brightness temperature eq. 2 can be rewritten as (Pritchard & Loeb 2012)

$$T_{21}(\hat{\mathbf{r}}, \nu) = 27 x_{\text{HI}} (1 + \delta_b) \left(1 - \frac{T_{\text{CMB}}}{T_s}\right) \left(\frac{1+z}{10} \frac{0.15}{\Omega_m h^2}\right)^{1/2} \left(\frac{\Omega_b h^2}{0.023}\right) \text{mK} \quad (5)$$

where  $\delta_b$  is the fractional baryon over-density,  $\Omega_m$ ,  $\Omega_b$  are the matter and baryon density parameters respectively, and the numerical factors are the result of an amalgamation of various constants.

In-depth pedagogical reviews on 21-cm cosmology can be found in Barkana (2016); Barkana & Loeb (2001); Furlanetto et al. (2006); Liu & Shaw (2020); Mesinger (2019); Pritchard & Loeb (2012).

## B. Cosmic history

### 1. Dark Ages ( $z \sim 1100 - 30$ )

After recombination (the decoupling of CMB photons at  $z \approx 1100$ ), the Universe entered the Dark Ages, before any stars or galaxies existed. During this era, neutral hydrogen filled the intergalactic medium (IGM) and the 21-cm spin temperature ( $T_s$ ) was governed by collisions with the cooling gas. Initially, Compton scattering off residual electrons kept the gas (and thus  $T_s$ ) thermally coupled to the CMB down to  $z \sim 300$ . Once this coupling broke, the gas cooled adiabatically faster than the CMB ( $T_{\text{gas}} \propto (1+z)^2$ ). With collisions still effective at high densities,  $T_s$  followed the gas temperature, dropping below the CMB temperature  $T_{\text{CMB}}$  and producing a 21-cm absorption signal against the CMB. By  $z \sim 30$ , however, the expanding gas became too diffuse for collisions to maintain coupling, so  $T_s$  drifted back toward  $T_{\text{CMB}}$ , causing the 21-cm signal to vanish (zero contrast). Throughout the Dark Ages, in the absence of astrophysical sources, the 21-cm fluctuations directly trace primordial density perturbations in the neutral hydrogen (assuming HI traces the underlying matter). This makes the Dark Ages 21-cm signal a pristine probe of fundamental cosmology (e.g. the matter power spectrum on small scales), potentially constraining inflationary parameters or dark matter properties (Loeb & Zaldarriaga 2004). In principle, observations of 21-cm from these ultra-high redshifts could shed light on new physics beyond the CMB (Scott & Rees 1990). In practice, detecting the Dark Ages signal is extraordinarily challenging: the relevant frequencies  $\nu \lesssim 50$  MHz are heavily contaminated by bright Galactic foregrounds and blocked by the ionosphere on Earth. As a result, this epoch remains unexplored observationally, reserved for futuristic instruments (perhaps a lunar radio array) capable of overcoming these hurdles (Tegmark & Zaldarriaga 2009).

### 2. Cosmic Dawn ( $z \sim 30 - 15$ )

The Cosmic Dawn began once the first generation of stars and galaxies formed (likely in halos of mass  $\gtrsim 10^5 - 10^6 M_\odot$ ). Lyman- $\alpha$  photons from these early luminous sources triggered the Wouthuysen-Field effect (Field 1958; Wouthuysen 1952): Ly $\alpha$  absorption and re-emission cycles flip the hydrogen spin, coupling  $T_s$  to the kinetic temperature of the cold IGM gas. As soon as a pervasive Ly $\alpha$  background developed,  $T_s$  was driven below  $T_{\text{CMB}}$  again, inducing a deep 21-cm absorption signal. This expected global absorption trough is the first prominent feature of the 21-cm history. Its depth and timing are sensitive to the onset of star formation and the Ly $\alpha$  production efficiency of the earliest galaxies. As Cosmic Dawn progresses, new radiative processes come into play: X-rays from the first X-ray binaries, mini-quasars, or hot interstellar gas begin to heat the IGM. These high-energy photons penetrate the IGM and photo-ionize atoms, depositing energy as heat via fast photo-electrons colliding with the gas. Gradually, X-ray heating raises the gas temperature. When the gas (and hence  $T_s$ ) is heated above the CMB temperature, the 21-cm signal transitions from absorption to emission. The precise redshift at which this turning point occurs depends on the total X-ray luminosity of early sources and the hardness of their spectra (Fialkov et al. 2014; Mirocha et al. 2017). Throughout Cosmic Dawn, the 21-cm brightness is highly inhomogeneous: regions near early galaxies see strong Ly $\alpha$  flux and early heating, while faraway regions remain colder and unheated. This patchiness encodes rich astrophysical information. Measuring the 21-cm signal (globally or via its power spectrum) during Cosmic Dawn would allow us to infer properties of the first sources: for example, the minimum halo mass able to host star formation, the stellar initial mass function, and the X-ray production efficiency (Pober et al. 2014). In essence, 21-cm observations during Cosmic Dawn directly probe the birth of the first stars and galaxies, opening a window on astrophysics at high redshift that was previously accessible only through theory.

### 3. Epoch of Reionization ( $z \sim 15 - 6$ )

As star formation accelerated, the Epoch of Reionization (EoR) unfolded, overlapping with the late stages of Cosmic Dawn. UV photons from young galaxies (and possibly quasars) gradually ionized the surrounding hydrogen gas, carving out growing ionized (HII) regions in the neutral IGM. Initially these ionized bubbles were small and isolated, but over time they expanded and merged. The volume-averaged neutral fraction of the Universe dropped from essentially unity to a few percent by the end of reionization. The 21-cm signal during the EoR became highly patchy. In neutral regions that were already heated ( $T_s \gg T_{\text{CMB}}$ ), the 21-cm line appeared in emission. In contrast, within ionized zones (or where gas was fully ionized), the 21-cm signal was absent entirely. Thus, 21-cm observations of the EoR can spatially map the distribution of neutral and ionized regions across the Universe. The characteristic size and growth of these 21-cm “bright” (neutral) and “dark” (ionized) patches inform us about the nature of reionization sources and the timeline of this phase transition (Friedrich et al. 2011; McQuinn et al. 2007). For instance, a rapid reionization would result in large, mergeable ionized regions appearing over a short interval, whereas a more extended reionization would produce a mix of bubble sizes over a longer period. Current observations (e.g. Gunn-Peterson troughs in  $z \sim 6$  quasar spectra and CMB polarization measurements) indicate reionization completed by  $z \approx 6-7$  (Ade et al. 2016; Fan et al. 2006). The 21-cm signal provides a direct probe of this process, in contrast to these indirect tracers. By measuring the 21-cm power spectrum or imaging the neutral hydrogen distribution, one can constrain the evolving ionizing photon budget and ionization topology – for example, determining the efficiency of galaxies in ionizing the IGM and the clumpiness of gas that absorbs these photons (Greig & Mesinger 2017; Robertson et al. 2010). In summary, the EoR 21-cm signal links cosmological structure formation with early galactic astrophysics, illuminating how the Universe’s diffuse gas was transformed from fully neutral to (almost) fully ionized.

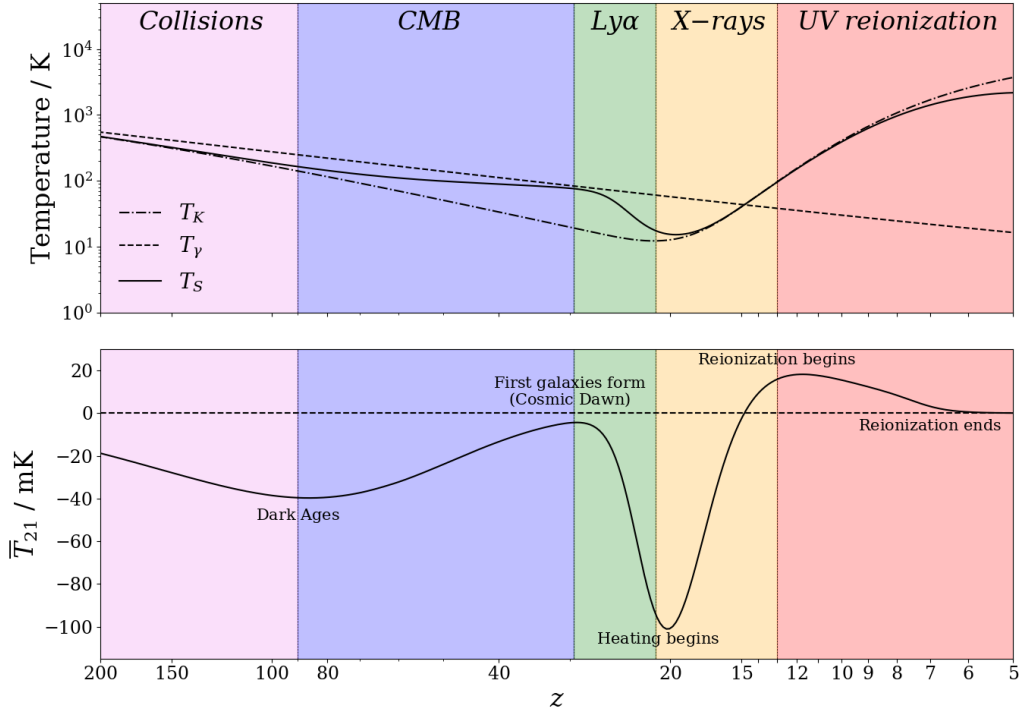


Fig. 1: An example plot of thermal history, with the global evolution of  $T_s$  and  $\bar{T}_{21}$  (defined in eq. 12 from redshift  $z \sim 200$  to  $z \sim 5$ , adopted with permission from Dhandha (2022)). The simulation package 21cmSPACE, discussed later, probes redshifts  $50 \gtrsim z \gtrsim 6$ .

### C. 21-cm observables

In astronomy, imaging a signal over a solid angle of sky is often seen as the holy grail of an experimental field. Unfortunately, in the case of 21-cm cosmology, this is inaccessible for a number of physical reasons. First and foremost, the 21-cm signal is extremely faint, with signals from the Epoch of Reionization often on the order of 1mK to 10mK. In contrast, a single radio-antenna system at  $\sim 150$  MHz (within the 50 to 250 MHz frequency band of HERA (DeBoer et al. 2017)) receives hundreds to thousands of kelvin of Galactic synchrotron emission and receiver noise. Because of this low signal-to-noise (SNR) ratio, there is not enough sensitivity to produce a high-fidelity image. In addition to this, recent experiments in 21-cm cosmology have heavily favoured interferometric approaches over single-dish approaches, due to the advantage that variable and vastly long baselines are essential in providing high angular resolution, as well as the statistical simplicity in data correlation – specifically, the lack of bias in estimation. However, interferometers inherently miss the total power unless single-dish auto-correlations are included, which is impractical in current experiments due to dominant receiver systematics (Liu & Shaw 2020).

Therefore, experiments in the field of 21-cm cosmology rely on statistical observations to inform the history of the Universe. The most important of these is arguably the *power spectrum*, whose measurement is the main focus for many current experiments (DeBoer et al. 2017). To define the power spectrum, first consider the three-dimensional Fourier transform from physical space to Fourier space, defined by

$$\tilde{T}(\mathbf{k}) \equiv \int_{-\infty}^{\infty} d^3r e^{-i\mathbf{k}\cdot\mathbf{r}} T(\mathbf{r}) \quad (6)$$

where  $\mathbf{r}, \mathbf{k}$  are comoving position and comoving wave- vectors respectively. The inverse transform is given by

$$T(\mathbf{r}) = \frac{1}{(2\pi)^3} \int_{-\infty}^{\infty} d^3k e^{i\mathbf{k}\cdot\mathbf{r}} \tilde{T}(\mathbf{k}). \quad (7)$$

The power spectrum can then be defined by the equation

$$\langle \tilde{T}(\mathbf{k}) \tilde{T}(\mathbf{k}')^* \rangle = (2\pi)^3 \delta^D(\mathbf{k} - \mathbf{k}') P(\mathbf{k}) \quad (8)$$

with  $\delta^D$  the Dirac delta function in  $D$  dimensions, and  $\langle \dots \rangle$  the ensemble average operation. Equivalently, and perhaps more intuitively, the power spectrum can be interpreted as the Fourier transform of the correlation function  $\xi(\mathbf{x}) \equiv \langle T(\mathbf{r}) T(\mathbf{r} - \mathbf{x}) \rangle$ , emphasizing the fact that the power spectrum measures correlations in configuration space, but simply is expressed in Fourier space:

$$\xi(\mathbf{x}) = \int \frac{d^3k}{(2\pi)^3} P(\mathbf{k}) e^{-i\mathbf{k}\cdot\mathbf{x}}. \quad (9)$$

This definition of the power spectrum includes the necessary information to completely statistically characterise a Gaussian random field (Coles 2001), which underlies inflationary models (Brandenberger 1985; Guth & Pi 1982). In cosmological literature, though, it is the quantity

$$\Delta^2(k) \equiv \frac{k^3}{2\pi^2} P(k) \quad (10)$$

which is more commonly seen. The reason for plotting this quantity  $\Delta^2$  instead of  $P(k)$  can be explained by considering the variance of a zero-mean random temperature field, as in, for example, the case of the mean-subtracted 21-cm brightness temperature field:

$$\begin{aligned}
\langle T^2(\mathbf{r}) \rangle &= \left\langle \left( \int_{-\infty}^{\infty} \frac{d^3 k}{(2\pi)^3} e^{i\mathbf{k}\cdot\mathbf{r}} \tilde{T}(\mathbf{k}) \right) \left( \int_{-\infty}^{\infty} \frac{d^3 q}{(2\pi)^3} e^{i\mathbf{q}\cdot\mathbf{r}} \tilde{T}(\mathbf{q}) \right)^* \right\rangle \\
&= \int_{-\infty}^{\infty} \frac{d^3 k}{(2\pi)^3} \frac{d^3 q}{(2\pi)^3} e^{i(\mathbf{k}-\mathbf{q})\cdot\mathbf{r}} \langle \tilde{T}(\mathbf{k}) \tilde{T}(\mathbf{q})^* \rangle \\
&= \int_{-\infty}^{\infty} \frac{dk^3}{2\pi^2} P(k) \\
&= \int_0^{\infty} d \ln k \Delta^2(k).
\end{aligned} \tag{11}$$

Therefore,  $\Delta^2(k)$  can be interpreted as the contribution to variance in configuration space in each logarithmic  $k$  bin.

While the power spectrum holds information about spatial fluctuations, it is also informative to investigate the *global signal*  $\bar{T}_{21}$ , defined as

$$\bar{T}_{21}(\nu) = \int d\Omega T_{21}(\hat{\mathbf{r}}, \nu). \tag{12}$$

As the notation suggests, this is an averaged quantity; specifically, it is the average power of the 21-cm signal across all sky angles, as a function of frequency.

## D. Initial conditions

### 1. Mass over-density fields

The current inflationary model of the Universe assumes that there existed some primordial power spectrum, imprinted at some arbitrarily early time (Coles 2001). The primordial power spectrum is defined by

$$P_0(k) = A_s \left( \frac{k}{k_*} \right)^{n_s-1}, \tag{13}$$

where  $k_*$  is the pivot scale  $0.002 \text{Mpc}^{-1}$ ,  $A_s$  the amplitude of the spectrum at the pivot scale, and  $n_s$  the scalar spectral index. This scalar spectral index represents the tilt of the power spectrum, with  $n_s = 1$  corresponding to the Harrison-Zeldovich spectrum (Harrison 1970; Zeldovich 1972), physically meaning that the power is scale invariant.

This primordial power spectrum is related to the power spectrum at each time through a *transfer function* (Bardeen et al. 1986). These phenomenological transfer functions mathematically encode how primordial density fluctuations are affected by processes such as radiation pressure, horizon entry, particle free-streaming (Coles 2001). Closed-form examples of fitting functions used as transfer functions can be found in, for example, Bardeen et al. (1986); Eisenstein & Hu (1998). As a function of wavenumber, the processed power spectrum  $P(k)$  relates to the primordial power spectrum  $P_0(k)$  through the transfer function  $\mathcal{T}(k)$  by the relation

$$P(k) = P_0(k) \mathcal{T}^2(k). \tag{14}$$

The power spectrum at each time dictates how the matter over-density field  $\delta_m$  itself are correlated.  $\delta_m$  is defined as a normalized deviation from the mean density:



$$\delta_m(t) = \frac{\rho(\mathbf{x}, t) - \bar{\rho}(t)}{\bar{\rho}(t)} \quad (15)$$

where  $\rho(\mathbf{x}, t)$  is the local matter density at position  $\mathbf{x}$  and time  $t$ , and the bar indicates an average over all space.

## 2. Streaming velocity effect

The streaming velocity effect is the result of the flows of baryons relative to the velocity of potential wells created by dark matter (Tseliakhovich & Hirata 2010). This effect is found to have non-negligible effects on structure formation: specifically, it suppresses the formation of haloes at small scales. This imprints on the 21-cm matter power spectrum as a decrease in power near Jeans scale (Tseliakhovich & Hirata 2010), which is the critical length scale at which density perturbations in gas clouds overcome pressure to gravitationally collapse (Jeans 1902). This Jeans scale  $\lambda_J$  depends on both the gas temperature and density, and is therefore indirectly sensitive to cosmology:

$$\lambda_J = \left( \frac{15k_b T}{4\pi G \mu \rho} \right)^{1/2} \quad (16)$$

where  $k_b$  is the Boltzmann constant,  $T$  is the gas temperature,  $G$  is the gravitational constant,  $\mu$  is the mean mass per gas particle and  $\rho$  is the mass density of the gas.

To define  $v_{bc}$ , the velocity divergence must first be defined as

$$\theta \equiv a^{-1} \nabla \cdot \mathbf{v} \quad (17)$$

where  $a$  is the dimensionless cosmological scale factor of the Universe, and  $\mathbf{v}$  is the velocity of either baryons or CDM. Then, the relative velocity is

$$\mathbf{v}_{bc} = \frac{\hat{k}}{ik} [\theta_b(\mathbf{k}) - \theta_c(\mathbf{k})] \quad (18)$$

where the subscripts  $b$  and  $c$  denote the  $\theta$  for baryons and CDM respectively. The power spectrum of  $v_{bc}$  is finally given by

$$\begin{aligned} \langle v_{bc}^2(\mathbf{x}) \rangle &= \int \frac{dk}{k} \Delta_\zeta^2(k) \left[ \frac{\theta_b(k) - \theta_c(k)}{k} \right]^2 \\ &= \int \frac{dk}{k} \Delta_{vbc}^2(k) \end{aligned} \quad (19)$$

where  $\Delta_\zeta^2(k)$  is the primordial curvature perturbation power spectrum.

### III. 21CMSPACE

For any physical system, simulations are an invaluable asset for a multitude of reasons, including generating mock data from mathematical theory, which can then be used for pipeline development and validation, as well as for foreground and instrumental modeling, which can then be used for experimental forecasting to inform instrument design.

However, evolving the early Universe on a machine is no easy task. Therefore, there does not exist one optimal way to simulate the period of time between recombination and reionization, but rather a multitude of different methods each with their own advantages and disadvantages. These methods lie on a spectrum with a trade off between accuracy and runtime. On one end lie numerical simulations such as *CoDa* (Ocvirk et al. 2015) and *LICORICE* (Semelin et al. 2017), which hold accuracy as its foremost priority. This is achieved through explicit evolution of structure formation using hydrodynamic theory (Gessey-Jones 2024), which can either be freshly written with the intent of simulating the 21-cm signal from nativity, or taken from a generic library upon which processes such as radiative transfer and chemical evolution can then be attached for the specific purpose of evolving the 21-cm observables. This approach, due to its theoretical ability to include a comprehensive suite of physical effects, advertises the best possible control over the processes at each evolution step. However, numerical simulations come with the heavy downside of computational cost. While it is true that computer performance is exponentially increasing alongside decreasing costs, the need and expectation for improvements in simulation accuracy, size, and resolution have continued to render purely numerical simulations too expensive both in computational power and time to perform large-scale explorations of parameter spaces.

On the other end of the spectrum are analytical simulations such as *ARES* (Mirocha 2014) and *Zeus21* (Muñoz 2023). In contrast to numerical simulations, analytical simulations do not explicitly evolve spatial volumes through time. Instead, they solve mathematical equations, which, using the plethora of numerical solution libraries available, can take less than a second using consumer hardware (Gessey-Jones 2024). However, this comes at the heavy trade-off of losing significant physical detail, with analytical equations having only the capability to model fields through averaged quantities, requiring significant approximations. Still, these calculations are of incredible value since these approximations are often subdominant compared to the inherently large observational error of the field. Despite their practical merit, though, the shortcomings of analytical simulations with regards to the lack of explicit evolution often prohibits output of full 21-cm signal maps or 21-cm power spectra.

Through the advantages and disadvantages of both numerical and analytical models, the need for a third class of simulations is hopefully clear: semi-numerical simulations. As the name suggests, semi-numerical simulations numerically resolve and evolve a spatial expanse, but rather than incorporating full hydrodynamic calculations of all processes at every step and every point in space, semi-numerical simulations invoke analytic calculations to deal with approximated quantities. Semi-numerical simulations therefore offer a compromise between accuracy and low computational cost. It is to this class of semi-numerical simulations that *21cmSPACE* belongs.

#### A. Design principles

*21cmSPACE* (21-cm Semi-numerical Predictions Across Cosmic Epochs<sup>1</sup>) is a code package developed by the Cambridge Cosmic Dawn Group over the past decade (Fialkov et al. 2012; Visbal et al. 2012). *21cmSPACE* evolves large-scale structure using analytic or perturbative solutions, while key astrophysical processes are included via parametric, sub-grid models and numerical integration where necessary. The core aim of *21cmSPACE* is to propagate the 21-cm brightness temperature field forward in time, in order to compute observable quantities such as the global (sky-averaged) 21-cm signal and its power spectrum. To

---

<sup>1</sup> This name was not given until mid-2023; older papers referring to this code do not include this name.

achieve this, the code self-consistently evolves all relevant fields – e.g., the hydrogen spin temperature  $T_s$ , the background radiation temperature  $T_{\text{CMB}}$ , the hydrogen neutral fraction  $x_{\text{HI}}$ , as well as derived quantities like star formation rates and radiation intensities.

By design, **21cmSPACE** divides the problem according to scale: large-scale intergalactic fields (such as mass density, streaming velocity, radiation backgrounds, and temperature) are evolved on a coarsely resolved simulation grid, while small-scale phenomena (halo collapse, star formation, feedback) are handled by sub-grid prescriptions. This separation of scales is the key to computational efficiency, without needing to sacrifice essential physical processes.

Several design philosophies underlie **21cmSPACE**. First, it emphasises flexibility in exploring astrophysical scenarios – a wide array of input parameters control star formation efficiencies, feedback strengths, spectral emissivities, etc., enabling the testing of different models of early Universe astrophysics. For example, the efficiencies of Pop II and Pop III star formation ( $f_{*,\text{II}}$ ,  $f_{*,\text{III}}$ ) and the delay time between Pop III and Pop II episodes ( $t_{\text{delay}}$ ) are all tunable inputs. Likewise, the relative X-ray luminosity of high- $z$  X-ray binaries ( $f_X$ ) and any additional radio background strength ( $f_r$ ) can be specified. Second, the code is structured for performance: any components of the calculation that do not depend on the specific astrophysical parameters are precomputed once and stored for reuse. This includes, for instance, cosmological tables, linear perturbation growth factors, and radiation window functions (used for fast radiative transfer). Third, **21cmSPACE** assumes a fixed cosmological model during a run (by default the Planck 2013  $\Lambda$ CDM parameters) and is optimized under that assumption. Overall, the architecture of **21cmSPACE** prioritizes physical fidelity (by including all major known 21-cm relevant processes) while maintaining speed through analytical treatments and precomputation. This makes it well-suited to produce rapid predictions of 21-cm observables across Cosmic Dawn and reionization for a range of scenarios.

## B. Code execution

Loosely, **21cmSPACE** applies the following set of instructions upon each execution (Gessey-Jones 2024):

1. A spatial volume is divided into cubical voxels of a specific side length, where the initial conditions of matter over-density field  $\delta_m(\mathbf{x})$  and the relative velocity field  $v_{bc}(\mathbf{x})$  are imposed.
2. Large-scale fields such as the Lyman-Werner field are initialized at the first time step from initial conditions, or computed from the previous time step.
3. These large-scale fields are used by sub-grid models within each voxel to calculate local properties, such as star formation prescription.
4. The local properties are then used to inform the large-scale fields, propagated by non-local processes such as radiative transfer.
5. Steps 2-4 are iterated until termination.

Temporally, **21cmSPACE** operates in redshift space with hard-coded endpoints, evolving from  $z = 50$  to  $z = 6$ . Across these redshifts, the Universe is described by linear perturbation theory. At  $z = 50$ , there is also negligible halo and star formation, permitting the use of the **CAMB**<sup>2</sup>(Lewis & Challinor 2011) and **Recfast**<sup>3</sup>(Seager et al. 2011) codes for the creation of initial conditions (Gessey-Jones 2024).

Spatially, the total size of **21cmSPACE** can be set to one of  $384^3$  cMpc<sup>3</sup>,  $768^3$  cMpc<sup>3</sup>, and  $1536^3$  cMpc<sup>3</sup> by changing the number of 3 cMpc side-length voxels to  $128^3$ ,  $256^3$ , and  $512^3$  respectively (Dhandha 2022).

---

<sup>2</sup> The Code for Anisotropies in the Microwave Background is a code for calculating various cosmological quantities, including power spectra and transfer functions.

<sup>3</sup> Recfast provides fast approximations for calculations of observables resulting from processes during the Epoch of Recombination, the era immediately preceding the period informed by 21-cm cosmology.

This largest simulation size of  $1536^3 \text{ cMpc}^3$  allows **21cmSPACE** to be useful in the forecasting for the SKA, whose beam covers a large enough square-angle at high redshifts to require this volume.

Additionally, the initial conditions are currently calculated from fixed parameters. In particular, **21cmSPACE** assumes the Planck 2013 best-fit  $\Lambda\text{CDM}$  model as a fixed cosmology (Ade et al. 2014). The initial over-density field  $\delta_m$  and baryon-dark matter relative velocity  $v_{bc}$  as defined in eq. 18 are computed (Fialkov et al. 2012) from the matter power spectrum and velocity power spectrum as output from **CAMB**, and the initial gas temperature and ionization fraction are calculated from the outputs provided by **Recfast**, both assuming Planck 2013.

In-depth descriptions of **21cmSPACE** and its parameters, simulation loop, and post-processing can be found in Gessey-Jones (2024); Gessey-Jones et al. (2023, 2024).

### C. Project motivation and impact

**21cmSPACE**, while being a powerful tool for simulation of the 21-cm signal, still holds some limitations. Particularly, as outlined in the previous section, despite there offering the option to include or exclude effects from a plethora of physical evolutionary processes, the instantiation of the simulation from its initial conditions remains confined to the use of its default Planck 2013 best-fit cosmology, and propagation thereof. This is an extremely strong assumption affecting many of the physical processes, either directly or by way of providing suitable environments at the right times, throughout the evolution of the 21-cm signal.

However, there is great value to be gained from the ability to evolve the 21-cm signal for variable cosmologies. As the amount of experimental data measuring various observable imprints of the 21-cm signal continues to increase, so too does the potential to use 21-cm data as a probe for constraining cosmological parameters. Specifically, the 21-cm signal depends on five cosmological parameters, summarized in Table I.

Parameter	Definition	Planck 2013 best-fit value
$h$	Dimensionless Hubble constant	0.6704
$\Omega_{\text{m},0}$	Dimensionless total matter (baryonic + dark) density at $z = 0$	0.3169
$\Omega_{\text{b},0}$	Dimensionless baryonic matter density at $z = 0$	0.0490
$\Omega_{\text{k},0}$	Dimensionless effective curvature density at $z = 0$	0
$T_{\text{CMB},0}$	Temperature of the Cosmic Microwave Background (CMB) at $z = 0$ in K	2.725

Table I: Cosmological parameters impacting the 21-cm signal, along with their definitions and 2013 best-fit values, as is included in the default settings of **21cmSPACE**.

The functionality to incorporate cosmological parameters into the inputs of **21cmSPACE** would be incredibly useful, and is the objective of a longer-term endeavour. A natural beginning towards this objective is the incorporation of cosmology dependence into the generation of initial conditions. These initial conditions are extremely sensitive to the underlying cosmology of the Universe, and their cosmology dependence is found to propagate significantly through the evolution of the 21-cm signal. The completion of this goal is a major step towards the full incorporation of cosmology dependence into the full simulation of the 21-cm signal.

In principle, the full incorporation of cosmology into **21cmSPACE** will enable exploration of the cosmological parameter space, relating each point in the space to a particular shape of the global signal and a particular shape of the power spectrum. Along with experimental data, the parameter space may then be constrained to narrow down possible locations for the true cosmology of the Universe. As well as this, the comparison of simulated signals with physical measurements will enable the verification or rejection of cosmological theories.

## IV. METHODOLOGY

### A. Initial conditions generation

The generation of initial conditions was done primarily in the pre-existing MATLAB function `get_IC_N`. The function took two inputs:  $N_{pix}$ , which represents the side-length of the total simulated spatial volume in number of pixels, and a random seed. The function then output two 3-dimensional scalar fields representing the  $\delta_m$  field and the  $v_{bc}$  field, defined in eq. 15 and eq. 18 respectively.

`get_IC_N` also further imported three precomputed files, each for a different redshift from  $\{40, 970, 1020\}$  containing transfer function data output by `CAMB`. In order to define the primordial power spectrum to be multiplied with these transfer functions as in eq. 13 and eq. 14, `21cmSPACE` used hard-coded values of  $A_s = 2.01664 \times 10^{-9}$  and  $n_s = 0.9675$ , consistent with the Planck2013 best-fit model (Ade et al. 2014). These values of  $A_s$  and  $n_s$  are responsible for the normalisation of the power spectra.

These transfer functions from each redshift are then used in `get_IC_N` to calculate the power spectra. To do this, they are passed through a smoothing window function defined by

$$W(k) = \exp\left(-\frac{k^2 R_w^2}{2}\right) \quad (20)$$

where  $R_w$  is a characteristic smoothing scale, chosen to be  $R_w = 1.7/\pi$  for the smoothing of 3 Mpc pixels. This window function serves the purpose of smoothing scales smaller than  $R_w$  in Fourier space, which correspond to higher  $k$  values. As well as this, the transfer functions are each multiplied by a factor of  $k^2$  so that they are roughly constant at super-horizon, low  $k$  modes. The total calculation for the matter power spectrum, taking into account the weighted sum of contributions from baryons and CDM, is straightforward albeit long:

$$P_m(k) = \frac{2\pi^2}{k^3} \Delta_\zeta^2(k) P_0(k) \left( W(k) \left[ \left( \frac{\Omega_b}{\Omega_m} k^2 \mathcal{T}_{\text{baryon}} \right) + \left( \frac{\Omega_m - \Omega_b}{\Omega_m} k^2 \mathcal{T}_{\text{CDM}} \right) \right] \right)^2. \quad (21)$$

where  $\Delta_\zeta^2(k)$  is again the primordial curvature perturbation power spectrum, set to a value of  $\Delta_\zeta^2(k) = 2.42 \times 10^{-9}$  (Dunkley et al. 2009).

The  $v_{bc}$  power spectrum, however, is more complex. First, the velocity divergences must be calculated as in eq. 17. This is impractical to do analytically; rather, in practice, the baryon velocity divergence is calculated using

$$\theta_b = \frac{H(z_{rec})}{c} (z_{rec} + 1) W(k) \frac{(\mathcal{T}_{\text{baryon}, 1020} k^2 - \mathcal{T}_{\text{baryon}, 970} k^2)}{50} \quad (22)$$

with  $z_{rec} = 1020$  the redshift of recombination at which the initial conditions are generated, and the 1020 and 970 subscripts denoting the redshift at which  $\mathcal{T}_{\text{baryon}}$  is evaluated. The CDM velocity divergence is calculated similarly, substituting the baryon transfer function for the CDM transfer function.

The relative velocity  $v_{bc}$  is then calculated according to the scalar form of eq. 18, appropriately scaling by the redshift:

$$v_{bc} = \frac{\theta_b - \theta_c}{ik(z_{rec} + 1)}. \quad (23)$$

Finally, the  $v_{bc}$  power spectrum is calculated explicitly:

$$P_{vbc} = \frac{2\pi^2}{k^3} P_0(k) \Delta_\zeta^2(k) v_{bc}. \quad (24)$$

After the matter power spectrum and relative velocity power spectrum have been explicitly calculated, the true generation of initial conditions may begin. First, a Gaussian random field is initialized in configuration space. Then, its Fourier transform is taken. Initializing in configuration space before taking the Fourier transform enforces Hermitian symmetry, which is essential for maintaining real (as opposed to complex) over-density fields. Further, the Gaussianity of the over-density fields is preserved due to the fact that the Gaussian distribution is an eigenfunction of the Fourier transform. Now, the power spectra can at last be imposed, scaling the random field in Fourier space to ensure that the perturbations match the cosmological model. This scaling is done using the same random variable base for the scalar  $\delta_m$ , as well as the  $v_{bc}$  along each of the three spatial dimensions separately. Finally, the Fourier space variables are inverse Fourier transformed back into configuration space. It is these configuration space boxes that are the final output of `get_IC.N`.

In order to implement variable cosmological parameters, `get_IC.N` was translated into Python. This decision was made for two reasons: firstly, the transfer functions used in the evolution of the power spectrum are output by `CAMB`, which is a code written mostly in Python. Secondly, the final implementation of variable cosmology in `21cmSPACE` strives to use the Python-based `astropy` module’s cosmology classes as an organizational tool for holding parameter values, as well as its object methods for performing standard cosmological calculations.

To receive information about cosmological parameters, the function `get_IC.N` was altered to take cosmology as an input parameter. Specifically, in addition to the two inputs of  $N_{pix}$  and random seed, `get_IC.N` takes a cosmology as a third parameter. This cosmology itself is defined by the five parameters in Table I.

Practically, the cosmology enters `get_IC.N` in two ways. Most obviously, the transfer functions encoding effects such as inflation and horizon interaction are sensitive to the cosmological parameters. While these were previously precomputed and saved in the interest of computational efficiency, they must be recalculated for every cosmology, and therefore it is logistically sensible for the calling of `CAMB` to be directly incorporated as a subroutine within `get_IC.N`. The execution of `CAMB`, from instantiation using parameters to the output of the transfer functions for each of the three redshifts required, takes on the order of seconds on consumer hardware when using `CAMB`’s default settings such as those governing the  $k$  range probed and the resolution of  $k$  sampling.

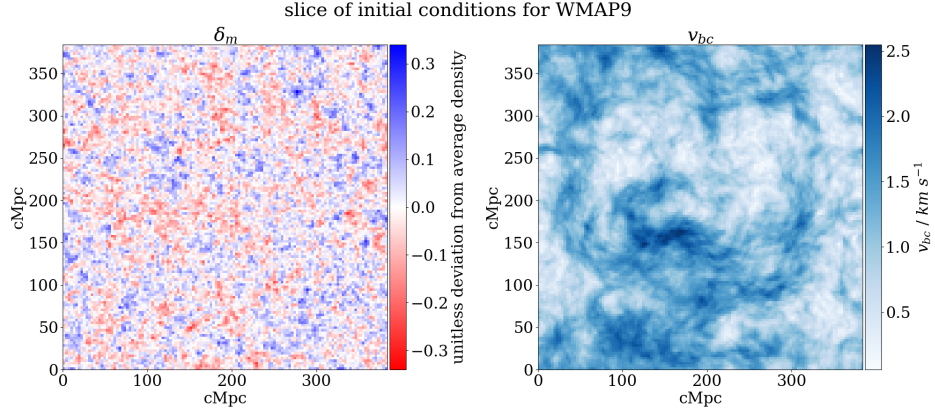
Those familiar with `CAMB` may be aware that `CAMB` now has the built-in functionality to output the power spectra directly, thus avoiding the need to manually scale and process the power spectrum from its primordial form. However, this was not an option at the time `21cmSPACE` was written. Still, though, the manual scaling of the power spectrum from transfer functions is implemented in the new Python version of the code as a design choice because the `CAMB` output power spectrum does not include the smoothing required at high  $k$  values. Additionally, manual scaling offers a level of control over the primordial power spectrum that sets up future work.

As well as this, the calculation of velocity divergence requires the value of Hubble parameter  $H$  at a specific redshift. This was previously done by implementing the FRW equation

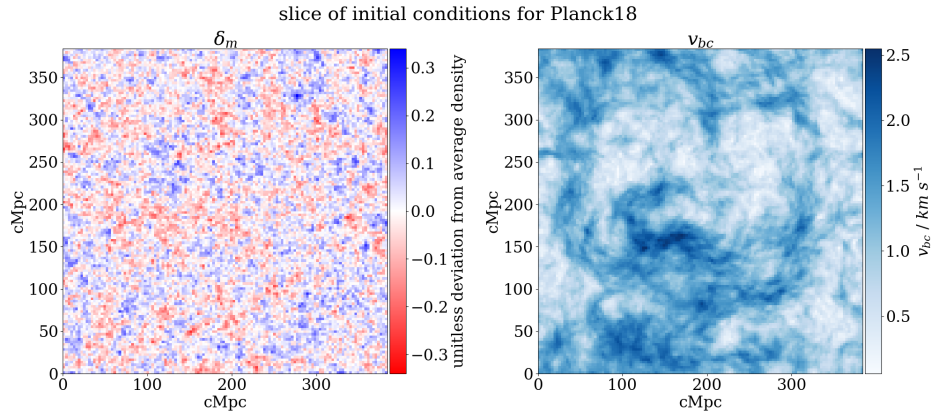
$$(H(z))^2 = H_0^2(\Omega_m(1+z)^3 + \Omega_\Lambda + \Omega_r(1+z)^4) \quad (25)$$

with hard-coded critical densities  $\Omega_m$  and  $\Omega_\Lambda$ , and the radiation pressure  $\Omega_r$  hard-coded to  $8.5522 \times 10^{-5}$  (Ade et al. 2014). To keep consistent with the input cosmology, this `get_H.z` method is now instead updated to use density values as provided by the given cosmology.

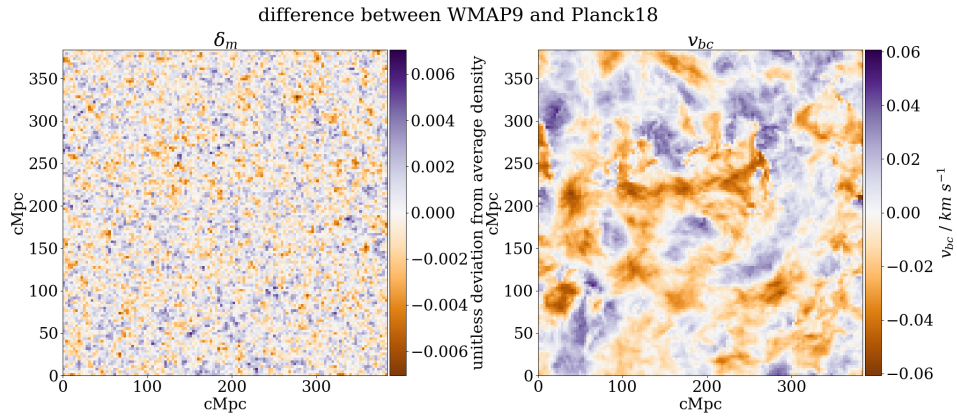
Since the new code is all written in the same language, a given random seed should cause all calculations to be deterministically performed. Therefore, any discrepancy in the initial condition grids must be due to a difference in the propagation of the cosmological parameters. This is illustrated in Fig. 2, which show a slice of initial condition boxes generated using the same random seed: the upper plots show that the initial conditions are, by eye, very similar (due to the deterministic nature of the random draws with a fixed seed). The lower plot, however, shows the difference in initial condition boxes, with deviations of up to  $\sim 5\%$ .



(a) A slice of the initial condition boxes for cosmology WMAP9 (Planck Collaboration et al. 2014) at redshift  $z = 50$ , with  $\delta_m$  on the left and  $v_{bc}$  on the right.



(b) A slice of the initial condition boxes for cosmology Planck 2018 (Planck Collaboration et al. 2020) at redshift  $z = 50$ , with  $\delta_m$  on the left and  $v_{bc}$  on the right.



(c) The differences between initial condition grids generated using WMAP9 and Planck 2018 with  $\delta_m$  on the left and  $v_{bc}$  on the right, calculated by subtracting the respective Planck 2018 slices in Fig. 2b from the WMAP9 slices in 2a.

Fig. 2: Fig. 2a and Fig. 2b show slices of initial condition boxes generated at redshift  $z = 50$  for the cosmologies using WMAP9 and Planck 2018 best-fit parameters respectively. Fig. 2c visualises the effect of altered cosmology by showing the difference between the two, exhibiting deviations of up to  $\sim 5\%$ .

## B. Consistency checks

Although the rewriting of code maintained the same mathematical algorithm, translating code from one language into another often introduces inconsistencies due to the nature of operating system and hardware interaction, or variations in implicitly-called library package subroutines. It is therefore important to perform consistency checks at every stage, in order to maintain confidence that the simulation is reflective of the underlying physics.

Due to the statistical nature of measurements, however, the stochasticity in the initialization of the random Gaussian field propagates through the imposition of the power spectrum, imprinting inherent randomness onto the final result. To complicate matters further, the generation of random Gaussian fields is non-identical between MATLAB and Python, even when using the same random seed.

It is therefore important to iterate the algorithm in both MATLAB and Python multiple times, and statistically compare the power spectra that these initial condition boxes produce. Specifically, after generating the initial condition boxes, the power spectrum can be computed independently from its generation. Taking each power spectrum from individual initial condition boxes, their average value at each  $k$  sample may be calculated as a best estimate of the power at that wavenumber; similarly, the standard deviation of the power value at each  $k$  sample may be used as an estimate of the uncertainty in the power, as a result of propagation of randomness from the initial Gaussian field. In principle, averaging an infinite number of iterations will return the original power spectrum which should perfectly agree with each other. However, in practice, each algorithm has an associated computational cost, limiting the number of samples; yet, as shown in Fig. 3, only as few as 10 runs is needed to clearly illustrate the agreement of the two code scripts with each other. The plots also include the fractional error, calculated by taking the absolute difference between the two methods, and then dividing by the legacy method's best estimate.

As is shown in the fractional error plots, the deviation between the legacy and new scripts is negligible; furthermore, all error bars overlap with 0% error, signifying that the legacy and new scripts, despite written in different languages and having different subroutines for the initialisation of Gaussian random fields, perform the same calculations and, more importantly, preserve the physics behind the computation.

The incorporation of **CAMB** into each execution of `get_IC_N` is also a potential source of deviation. As **CAMB** is an independently maintained code package, it is possible that **CAMB** has undergone changes in its parameters, calculation, or post-processing over the decade since the original legacy precomputed transfer functions used in `get_IC_N` were written to file. Therefore, it is useful to check that `get_IC_N`'s output, when using the legacy code with hard-coded Planck 2013 parameters, is consistent with the new code when directly calling **CAMB**, also using Planck 2013 parameters. The comparisons are shown in Fig. 4.

The fractional error plot in  $v_{bc}$  shows all error bars overlapping with 0 error; therefore, the  $v_{bc}$  calculation when incorporating **CAMB** can be taken to be statistically identical. However, fractional error in the  $\delta_m$  power spectrum shows an error of about 3%,

The fractional error plot in Fig. 4 for both  $v_{bc}$  and  $\delta_m$  show negligible error at low  $k$  modes (large scales), but at high  $k$  modes (small scales) deviations of  $\sim 3\%$ . Although nonzero, an error of  $\sim 3\%$  is negligible in the scheme of instrumental errors in current 21-cm cosmological experiments. Therefore, together, the consistency checks in Fig. 3 and Fig. 4 are enough to approve the use of the **CAMB**-incorporated Python version of `get_IC_N` into 21cmSPACE.



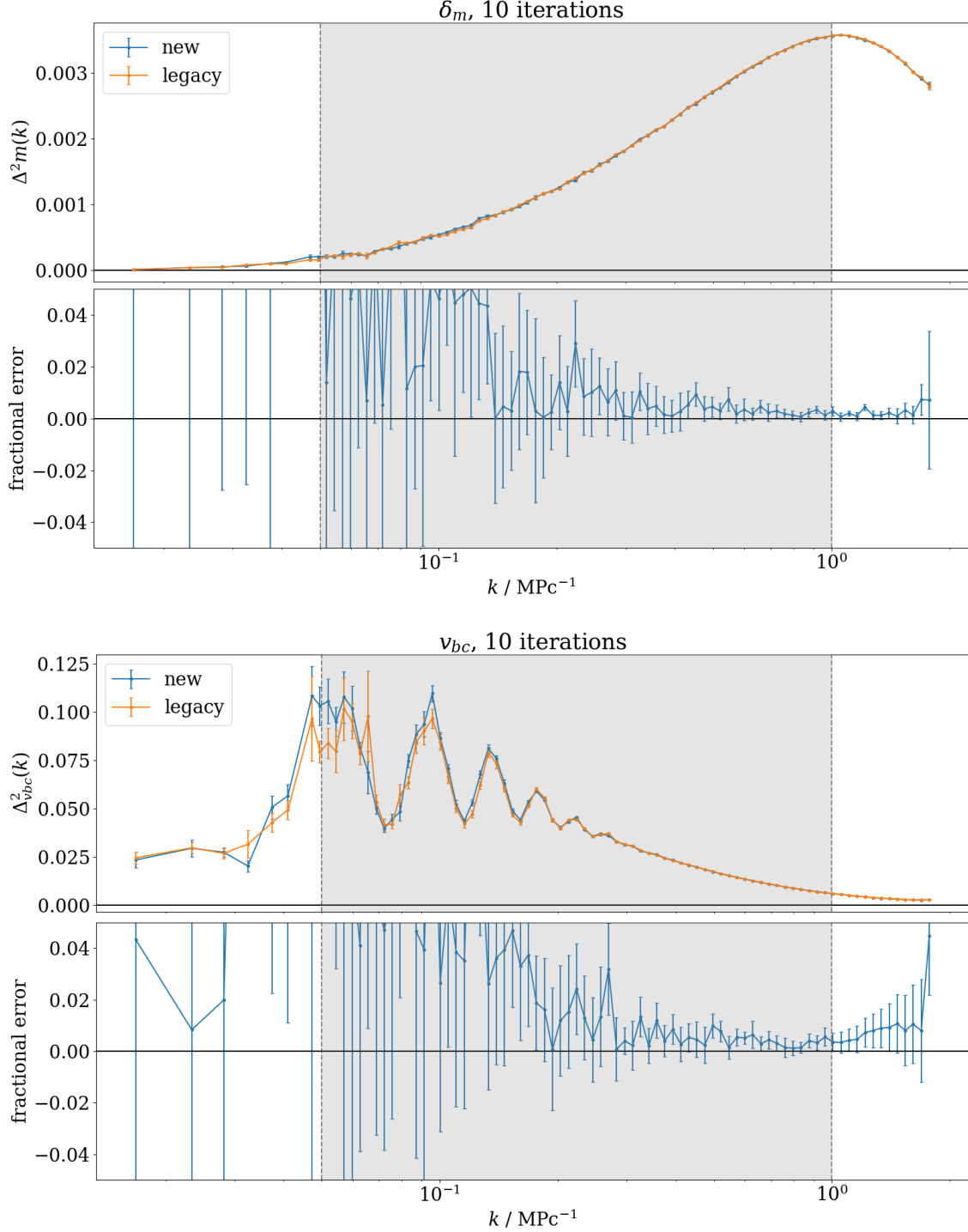


Fig. 3: The upper axes in each pair of plots show a comparison of power spectra between legacy and new initial condition generation scripts, **before** the incorporation of CAMB. The initial conditions are generated at redshift  $z = 50$ , for cubical voxels of 3 cMpc sidelength. The x-axis is shared for each pair of plots, and the shaded region is the domain of  $k$ -space probed by 21cmSPACE, limited at the small scale by resolution and at the large scale by total simulation volume. Best estimates are calculated using the average of power at each  $k$  sample over 10 iterations to smooth out effects from randomness in the initial Gaussian draws, and error bars are calculated by taking the standard deviation of the same quantity and dividing by the square root of the number of iterations. The lower axes show the fractional error between the two scripts with errors from the two sources properly propagated, treating the legacy script as truth. The comparison for both  $\delta_m$  and  $v_{bc}$  show no significant difference.

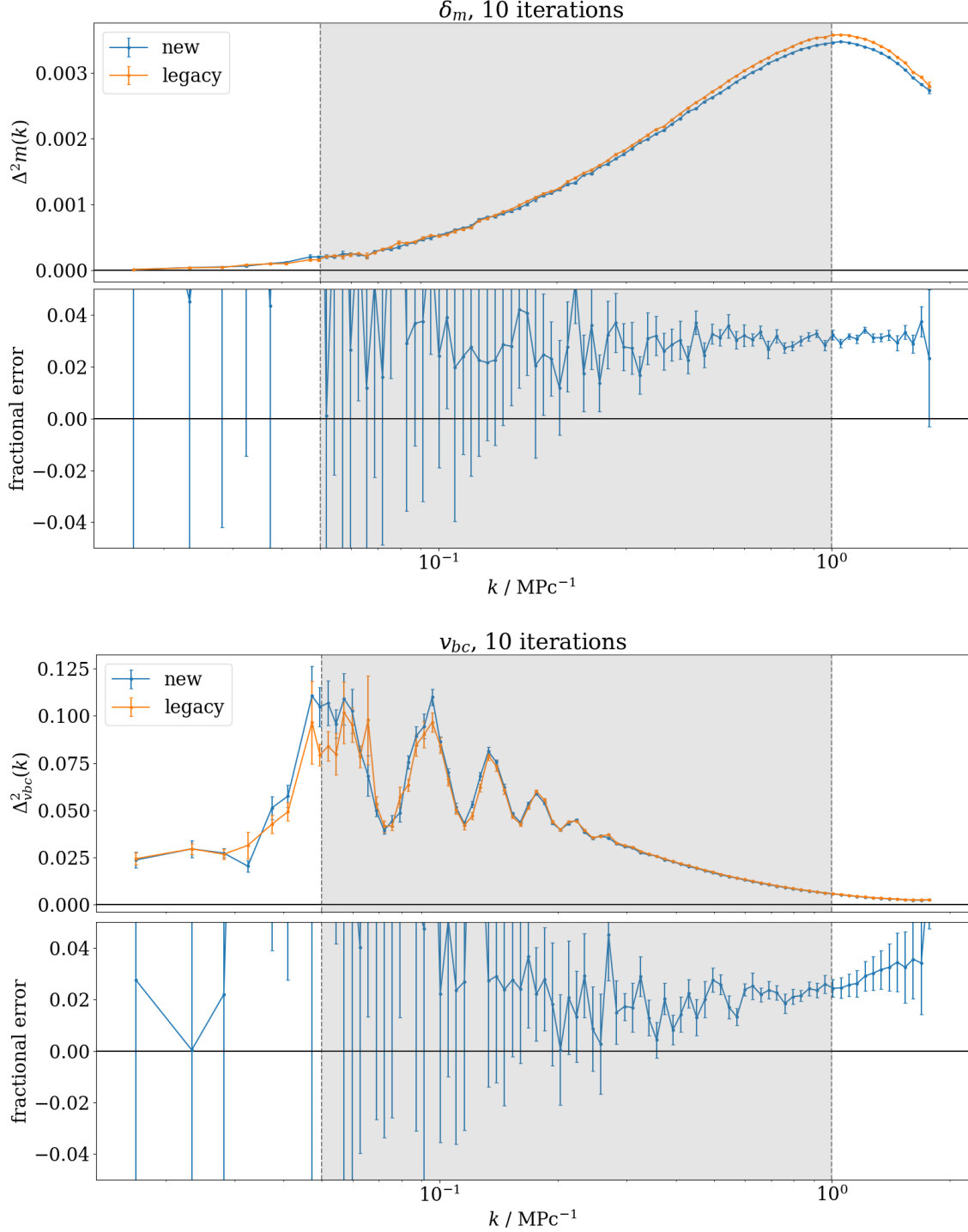


Fig. 4: The upper axes show a comparison of power spectra between legacy and new initial condition generation scripts, **after** the incorporation of CAMB. The initial conditions are generated at redshift  $z = 50$ , for cubical voxels of 3 cMpc sidelength. The x-axis is shared for each pair of plots, and the shaded region is the domain of  $k$ -space probed by 21cmSPACE, limited at the small scale by resolution and at the large scale by total simulation volume. Best estimates are calculated using the average of power at each  $k$  sample over 10 iterations to smooth out effects from randomness in the initial Gaussian draws, and error bars are calculated by taking the standard deviation of the same quantity and dividing by the square root of the number of iterations. The lower axes show the fractional error between the two scripts with errors from the two sources properly propagated, treating the legacy script as truth. The comparison for both  $\delta_m$  and  $v_{bc}$  show deviation of  $\sim 3\%$ , which is significant but subdominant to instrumental error of current experiments.

## V. RESULTS AND DISCUSSION

### A. Simulation suite

With the infrastructure for cosmology-dependent initial conditions successfully implemented, **21cmSPACE** was executed using the Planck 2018 best-fit parameters (Planck Collaboration et al. 2020) in the generation of  $\delta_m$  and  $v_{bc}$  initial grids. As well as this, **21cmSPACE** was also run using initial conditions generated with custom cosmologies. In principle, it is possible to vary any of the parameters as outlined in Table I; in this example study, the three parameters  $\Omega_m$ ,  $\Omega_b$  and  $h$  are varied one at a time while holding all other parameters constant to the Planck 2018 best-fit value where physically possible ( $\Omega_{de}$  varies based on the value of  $\Omega_m$  to keep  $\Omega_m + \Omega_{de} + \Omega_r = 1$  for a flat universe, and varies slightly based on  $h$  due to its propagation through the critical density). Their parameter values are summarized in Table II. The names of the custom cosmologies are arbitrary, and the values were chosen somewhat freely to provide a range centred near the best-fit Planck 2018 parameters. This freedom is acceptable – the intention of the following section is to demonstrate sensitivity of the 21-cm signal to cosmological dependence in initial conditions, as well as success in code infrastructure implementation.

Cosmology	$h$	$\Omega_m$	$\Omega_b$	$\Omega_{dm}$	$\Omega_{de}$	$T_{\text{CMB}} / \text{K}$
Planck18	0.6766	0.30966	0.04897	0.26069	0.68885	2.7255
Om1	0.6766	<b>0.1</b>	0.04897	0.05103	0.89991	2.7255
Om2	0.6766	<b>0.2</b>	0.04897	0.15103	0.79991	2.7255
Om3	0.6766	<b>0.3</b>	0.04897	0.25103	0.69991	2.7255
Om4	0.6766	<b>0.4</b>	0.04897	0.35103	0.59991	2.7255
Om5	0.6766	<b>0.5</b>	0.04897	0.45103	0.49991	2.7255
Ob3	0.6766	0.30966	<b>0.03</b>	0.27966	0.69025	2.7255
Ob4	0.6766	0.30966	<b>0.04</b>	0.26966	0.69025	2.7255
Ob5	0.6766	0.30966	<b>0.05</b>	0.25966	0.69025	2.7255
Ob6	0.6766	0.30966	<b>0.06</b>	0.24966	0.69025	2.7255
Ob7	0.6766	0.30966	<b>0.07</b>	0.23966	0.69025	2.7255
h5	<b>0.5</b>	0.30966	0.04897	0.26069	0.69017	2.7255
h6	<b>0.6</b>	0.30966	0.04897	0.26069	0.69022	2.7255
h7	<b>0.7</b>	0.30966	0.04897	0.26069	0.69025	2.7255
h8	<b>0.8</b>	0.30966	0.04897	0.26069	0.69027	2.7255
h9	<b>0.9</b>	0.30966	0.04897	0.26069	0.69029	2.7255

Table II: Cosmological parameters used in executions of **21cmSPACE**. The cosmological parameter varied is in blue; parameters which are not varied are held constant to Planck 2018 values (Planck Collaboration et al. 2020) wherever physically sensible.

Sample plots of slices of the initial condition boxes are shown in Fig. 5. Some differences are visually obvious: the  $\delta_m$  power spectrum amplitude is hugely suppressed in Om1 compared to Om5, and the correlation in  $v_{bc}$  is suppressed on smaller length scales in Om1 when compared to Om5. This behaviour is expected, since higher density matter results in matter generally being clumped together, and hence being able to correlate more finely.

This is consistent with the matter power spectra shown in the top row of Fig. 6: the power in both  $\delta_m$  and  $v_{bc}$  generally monotonically increase with higher  $\Omega_m$ , at least within the  $k$  domain of interest. One thing to note is that the power spectrum in  $v_{bc}$  also experiences some horizontal shifting towards higher  $k$  (corresponding to smaller length scales) with higher  $\Omega_m$ , which continues to be consistent with the previous physical reasoning.

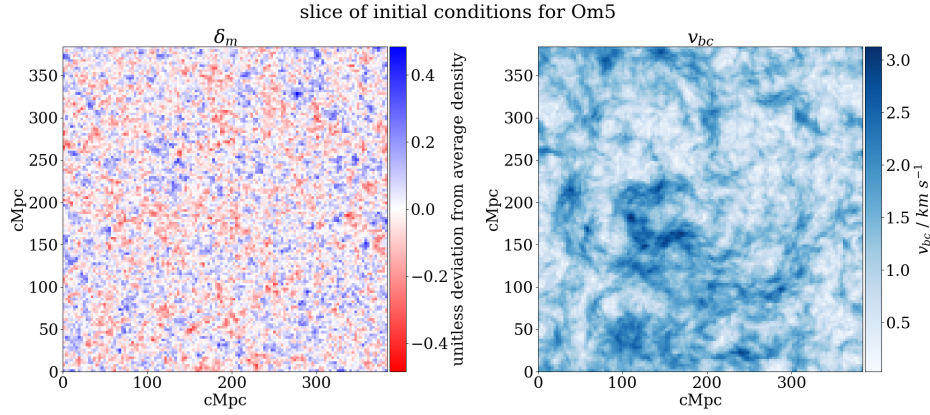
Along with this, power spectra for varying  $\Omega_b$  are shown in the middle row of Fig. 6. This time, power appears to instead decrease with increasing  $\Omega_b$ , both in  $\delta_m$  and  $v_{bc}$ . In contrast to  $\Omega_m$ , though, varying  $\Omega_b$  leaves the does not appear to have as much of an effect on the redistribution of  $v_{bc}$  power to different scales,

but rather mostly changes only the amplitude.

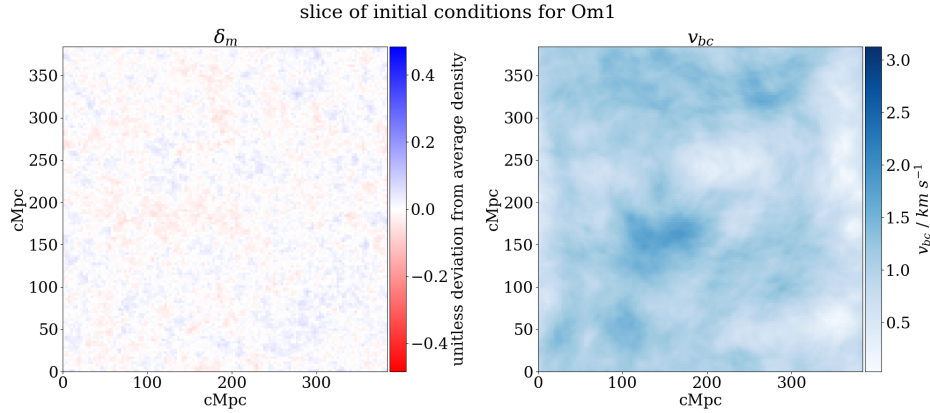
Finally, the power spectra for varying  $h$  are shown in the bottom row of Fig. 6, which shows an increase in power for both  $\delta_m$  and  $v_{bc}$  with increasing  $h$ , as well as another shift of power towards higher  $k$  with increasing  $h$ .

It is important to note that the cosmology is not yet altered in the evolutionary phase of 21cmSPACE – all differences shown in later sections are a result only of the dependence of initial conditions on cosmology.

For each varied parameter, the global signal  $\bar{T}_{21}$  is plotted. Additionally, the 21-cm power spectra  $\Delta^2(k)$  are plotted at fixed redshifts of  $z = 40$  and  $z = 20$ , as well as at fixed wavenumber  $k = 0.1 \text{ Mpc}^{-1}$  and  $k = 1 \text{ Mpc}^{-1}$ . These redshifts were chosen because at  $z = 40$ , the Universe is still sparse and large scale structure has yet to take place, so the power spectra here provide clear insight into the structure at very early times; in contrast, by  $z = 20$ , the Universe is undergoing various physical processes during heating and therefore the power spectrum provides a window to the timing and evolutionary stage of the Universe. Likewise, the wavenumbers  $k = 0.1 \text{ Mpc}^{-1}$  and  $1 \text{ Mpc}^{-1}$  were chosen because they are at opposing ends of the scales probed by 21cmSPACE; therefore, the power spectra at these wavenumbers is informative of structure formation both at the large and small scales.



(a) A slice of the initial condition boxes for custom cosmology Om1 at redshift  $z = 50$ , with  $\delta_m$  on the left and  $v_{bc}$  on the right.



(b) A slice of the initial condition boxes for custom cosmology Om5 at redshift  $z = 50$ , with  $\delta_m$  on the left and  $v_{bc}$  on the right.

Fig. 5: Sample slices of initial condition boxes for the custom cosmologies Om1 and Om5 both at redshift  $z = 50$ , shown in 5b and 5a respectively. The suppression of the matter power spectrum in  $\delta_m$  and lack of smaller-scale correlation in  $v_{bc}$  is clearly visible for the Om1 case, compared to Om5.

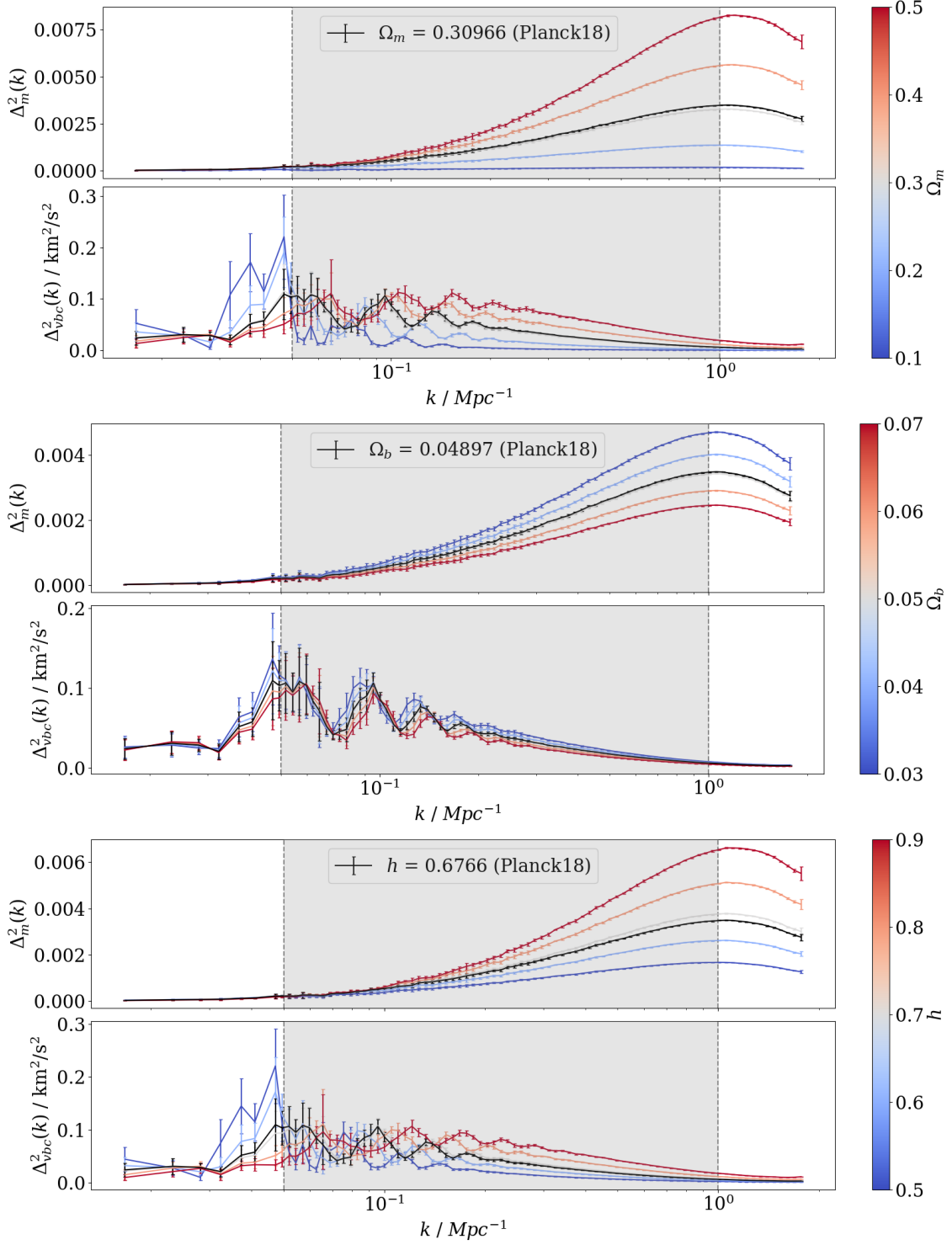


Fig. 6: Matter over-density power spectra  $\Delta_m^2$  and  $v_{bc}$  power spectra  $\Delta_{vbc}^2$  for custom cosmologies (colorbar with higher values in red and lower values in blue, and parameters as specified in Table II) and Planck 2018 best-fit parameters (black). The x-axis is shared between each pair of plots for each cosmological parameter. The shaded region is the domain of  $k$ -space probed by 21cmSPACE, limited at the small scale by resolution and at the large scale by total simulation volume. Although  $\Delta_m^2$  is usually shown in logarithmic axes, they are shown here in linear axes to show the difference between cosmologies.

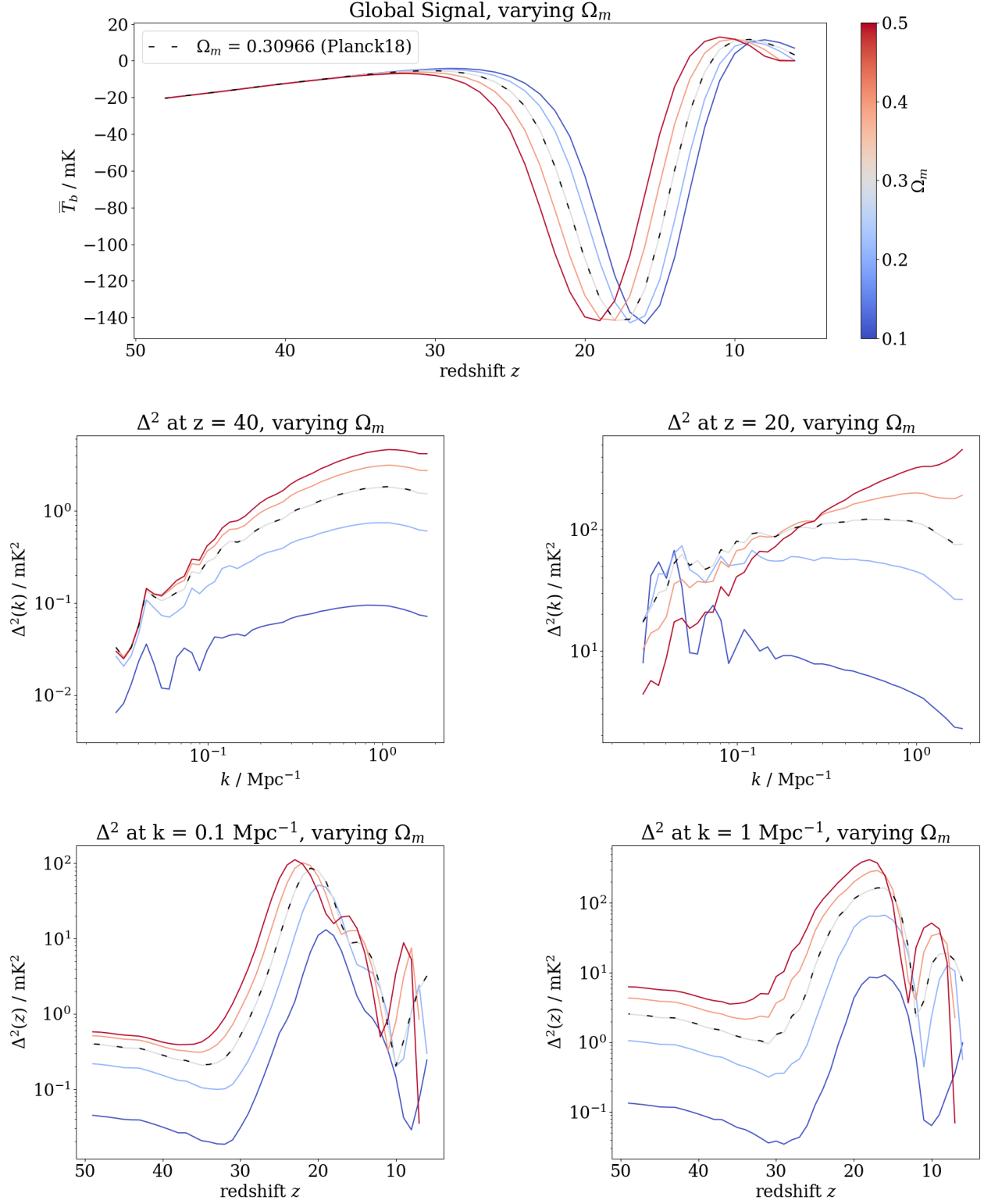
B. Varying  $\Omega_m$ 

Fig. 7: For custom cosmologies varying the value of  $\Omega_m$ , the 21cmSPACE simulated 21-cm global signal (top row), the simulated 21-cm matter power spectrum at fixed  $z$  (middle row:  $z = 40$  on the left and  $z = 20$  on the right), and the simulated 21-cm matter power spectrum at fixed  $k$  (bottom row:  $k = 0.1$  Mpc<sup>-1</sup> on the left and  $k = 1$  Mpc<sup>-1</sup> on the right). The colorbar indicates the value of  $\Omega_m$  and Planck 2018 values are in black.

Out of the three cosmological parameters varied,  $\Omega_m$  induces the most pronounced effect in the output of the 21-cm global signal, as shown in the top row of Fig. 7. Most notably, the centring of the absorption trough is significantly shifted towards higher redshift for higher values of  $\Omega_m$ . As well as this, the depth of the absorption trough is marginally shallower for higher values of  $\Omega_m$ , and the amplitude of the emission bump is also smaller for higher  $\Omega_m$ . The Planck 2018 best-fit cosmology, which uses a value of  $\Omega_m = 0.30966$ , produces a curve very similar to that of the cosmology using  $\Omega_m = 0.3$ , which serves as a convenient consistency check.

Since the global signal is an imprint of the thermal and ionization history of the IGM during Cosmic Dawn and the EoR, it is highly sensitive to the timing of star formation and heating processes. Varying the matter density  $\Omega_m$  has the effect of dictating when structure formation primarily occurs. When the value of  $\Omega_m$  is low, the Universe is less dense; therefore, the density fluctuations take more time to grow, delaying the collapse of the first haloes and therefore the formation of the first stars. This delay causes Ly $\alpha$  coupling to also be delayed, occurring at lower redshifts when the gas has further cooled and the CMB temperature is lower. Therefore, the absorption trough in the global signal, which arises due to  $T_s$  dropping much below  $T_{\text{CMB}}$ , is deeper and centred at later time (lower  $z$ ). On the other hand, a high  $\Omega_m$  universe collapses structure earlier and more efficiently. Hence, stars form earlier and the cosmic gas is heated by starlight earlier (higher  $z$ ). This leads to earlier coupling and X-ray heating: the absorption trough for  $\Omega_m = 0.5$  is at higher redshift and is also slightly shallower, since early X-ray photons begin heating the cold IGM sooner, while  $T_{\text{CMB}}$  is still higher.

In all cases, when X-ray heating becomes efficient, the global brightness temperature rises. Since a higher  $\Omega_m$  causes a higher star formation rate at each time, a higher  $\Omega_m$  cosmology causes the IGM to be heated more rapidly. Therefore, the trough is narrower (as seen by larger spacing between the curves during falling temperatures, compared to rising temperatures). Similarly, reionization, which is driven by UV radiation from galaxies, begins at different times: in the high  $\Omega_m$  cases, the higher density of galaxies at early times ionize the IGM faster, ending the 21-cm signal slightly earlier. On the other hand, lower  $\Omega_m$  cases show delayed reionization, shifting the signal beyond that of the simulation domain of 21cmSPACE (later than  $z = 6$ ). Physically, higher matter content should accelerate the buildup of the ionizing background, while lower density postpones it.

The effect of varied  $\Omega_m$  on the power spectrum, however, is less simple. The second row of Fig. 7 shows slices of the 21-cm power spectra at specific values of  $z$ , as a function of  $k$ . At  $z = 40$ , little to no star formation has occurred in any cosmology (as can be seen in the lack of deviation between curves in the global signal). The power spectra are thus reflective almost exclusively of the initial conditions themselves, closely resembling the curves in the middle row of Fig. 6. The high  $\Omega_m$  cosmologies have significantly higher power on small scales (high  $k$ ) than the low  $\Omega_m$  cases, since the higher matter density enables more correlation at these smaller length scales.

By  $z = 20$ , however, the impact of various astrophysical processes is far more significant, and the differences between cosmologies are a result of both the deviations in initial conditions and the differences in star formation rates. At this later redshift, all models are in the midst of Cosmic Dawn: the first generations of stars have formed and emitted Ly $\alpha$  and X-rays. This induces patchy heating and coupling, as illustrated by the shallower or even negative gradient of the power spectra on small to mid-length scales ( $k \sim 0.1 - 1 \text{ Mpc}^{-1}$ ). This patchy heating is a result of halo formation, which occurs at earlier times in higher  $\Omega_m$  cosmologies, hence the higher power in high  $\Omega_m$  cosmologies compared to low  $\Omega_m$  cases. The shapes of the curves also shed light on the length scales of these haloes: in low  $\Omega_m$  cases, the power spectrum peaks around  $k \sim 0.3 \text{ Mpc}^{-1}$ , indicating heated regions on the scale of a few Mpc; instead, the high  $\Omega_m$  cases show high power all the way until  $k \gtrsim 1 \text{ Mpc}^{-1}$ , indicating more structure at sub-Mpc scales.

The last row of Fig. 7 instead shows an orthogonal slice of the 21-cm power spectra, at fixed values of  $k$  varying over  $z$ . Each 21-cm power spectrum exhibits peaks around redshift  $z = 20$  and  $z = 10$ , corresponding most notably to the Cosmic Dawn and the EoR. As is consistent with the 21-cm global signal, varying  $\Omega_m$  alters the timing and width of these peaks by changing the process of structure formation. The differences in these power spectra are far larger at large  $k$  than at small  $k$  (more different at small scales than large scales) which is expected, since both X-ray heating and reionization are results of small scale galactic sources.

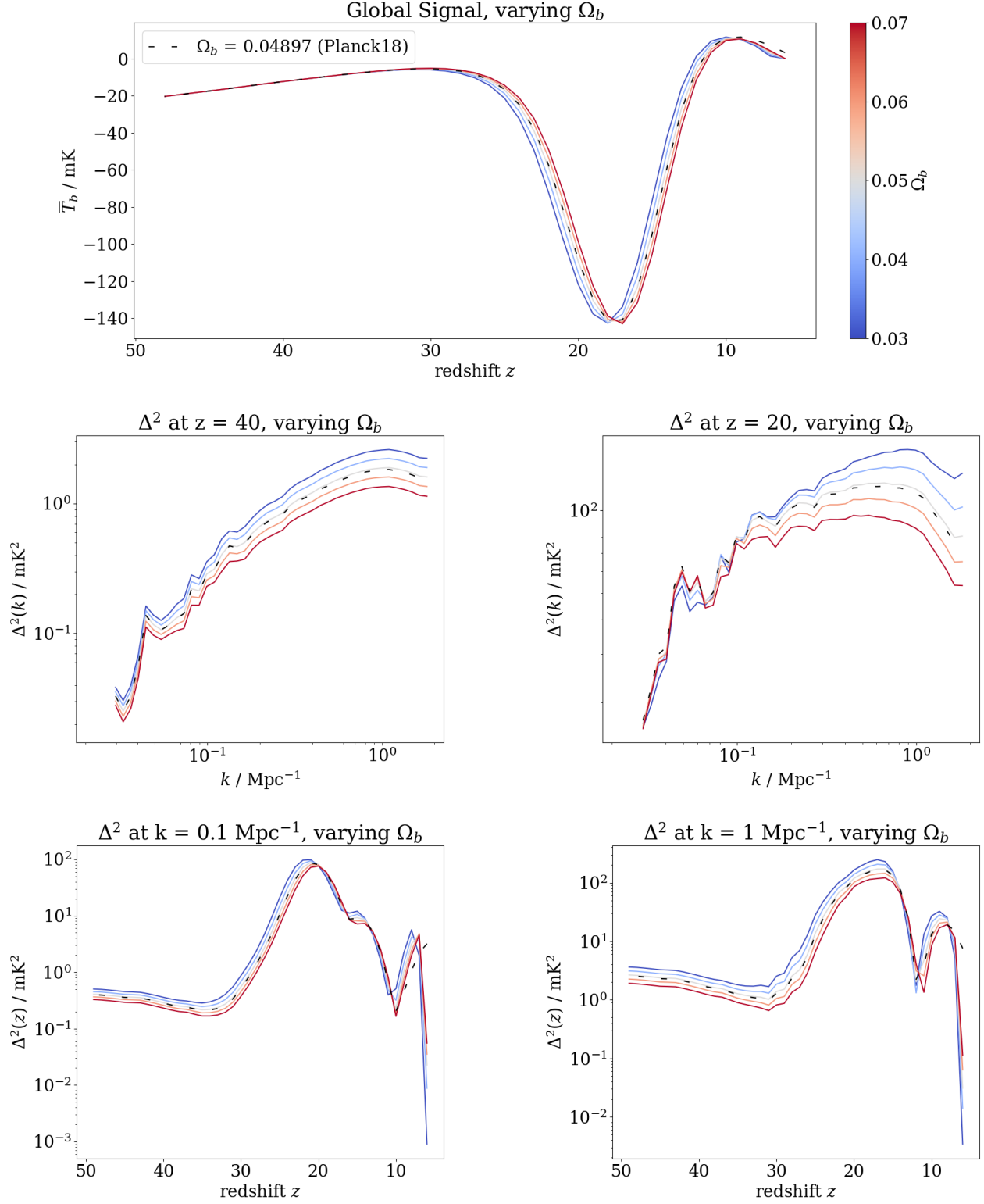
C. Varying  $\Omega_b$ 

Fig. 8: For custom cosmologies varying the value of  $\Omega_b$ , the 21cmSPACE simulated 21-cm global signal (top row), the simulated 21-cm matter power spectrum at fixed  $z$  (middle row:  $z = 40$  on the left and  $z = 20$  on the right), and the simulated 21-cm matter power spectrum at fixed  $k$  (bottom row:  $k = 0.1 \text{ Mpc}^{-1}$  on the left and  $k = 1 \text{ Mpc}^{-1}$  on the right). The colorbar indicates the value of  $\Omega_b$  and Planck 2018 values are in black.



Varying  $\Omega_b$  also shifts the timing and amplitude of the absorption trough (the first row of Fig. 8), albeit to a lesser degree than the variation of  $\Omega_m$ . The dependence is also different: whereas increases in both  $\Omega_m$  and  $\Omega_b$  cause the absorption trough to become slightly deeper, a larger value of  $\Omega_m$  causes the absorption trough to reach a minimum earlier, as opposed to an increase  $\Omega_b$  which causes the trough to shift later in the 21-cm evolution. The fiducial curve using the Planck 2018 value of  $\Omega_b = 0.04897$  lies very close to the  $\Omega_b = 0.05$  case, as expected.

It is interesting to note that the results in these power spectra partially subvert expectations: while a higher baryon density should naively provide higher power, this result instead generally suggests the opposite. This possibly stems from the fact that the code is not yet self-consistent, and takes the default Planck value of  $\Omega_b$  during the evolution. Therefore, the overall effect of changing  $\Omega_b$  in the initial conditions is simply to suppress the matter power spectra, instead of explicitly altering the baryon fraction. Still, this result is insightful because shows that the suppression of the matter power spectra in the middle row of Fig. 6, arising from the increase in baryonic pressure and independent of 21cmSPACE propagation inconsistencies, imprints a significant difference in the signal.

As shown in the top row of Fig. 8, the timing of the absorption trough is shifted later to lower redshift for larger values of  $\Omega_b$ . This is because raising  $\Omega_b$  while holding  $\Omega_m$  constant necessarily reduces the cold dark matter fraction ( $\Omega_{dm}$ , as in Table II). Thus, halos form later with more baryonic pressure, and the onset of Ly $\alpha$  coupling and heating occurs at lower redshift. This result should be interpreted with caution, however, since implementing consistent values of  $\Omega_b$  throughout evolution of the 21-cm signal could alter this effect.

The depth of the absorption trough could also change further: on one hand, the trough could become deeper since differential brightness temperature (i.e., contrast) scales with  $\Omega_b$ , as in eq. 5. In addition, the optical depth  $\tau_{21}$  in eq. 4 scales with hydrogen atom number density, which naturally increases with higher  $\Omega_b$ . This should lead to deeper absorption when the gas cools, and stronger emission when the gas heats. On the other hand, a higher baryon density also decreases the optical depth, thereby decreasing the contrast visible in the global signal trough. Implementation of consistent  $\Omega_b$  will reveal which of these factors is dominant.

The second row of Fig. 8 shows power spectra at fixed  $z$  as functions of  $k$ , for various values of  $\Omega_b$ . Again, at  $z = 40$ , the 21-cm power spectra are generally still reflective of the mass over-density power spectra in the middle row of Fig. 6. Higher  $\Omega_b$  decreases the 21-cm power spectrum amplitude, since an increase in  $\Omega_b$  leads to overall suppression of the initial matter power spectrum. The propagation of this suppression to the 21-cm power spectrum leads to somewhat uniform decreases in power across all scales, with only minor changes in the spectrum shape arising from an increase in  $\Omega_b$  raising the baryonic pressure within matter clumps, thereby increasing the Jeans scale and leading to a small suppression at high  $k$ .

The effect of this increase in the Jeans scale is far more pronounced at  $z = 20$ . At this redshift, when the Universe is partly coupled to the first sources, the suppressed initial matter power spectra still results generally in suppressed power over all scales. At higher  $k$ , though, the increase in Jeans scale is more pronounced – the higher pressure increases the general size of matter clumps. Conversely, because haloes cluster slightly less strongly when dark matter density is reduced, the relative power at small  $k$  can rise marginally. Therefore, in addition to power scaling, this shift in power from large  $k$  to small  $k$  (small length scales to large length scales) results in a reshaping of the power spectrum.

The physics is further apparent in the bottom row of Fig. 8: the delay in star formation induced by higher  $\Omega_b$  reducing  $\Omega_{dm}$  and hence physically lowering the number of dark matter haloes can clearly be seen, resulting in rightward shifts of the curves toward lower redshift and a reduction in power over both small and large scales. Because of the previously mentioned shift in power from large  $k$  to small  $k$ , the impact of increasing  $\Omega_b$  is more pronounced at higher  $k$ , evidenced by the larger spacing between curves.

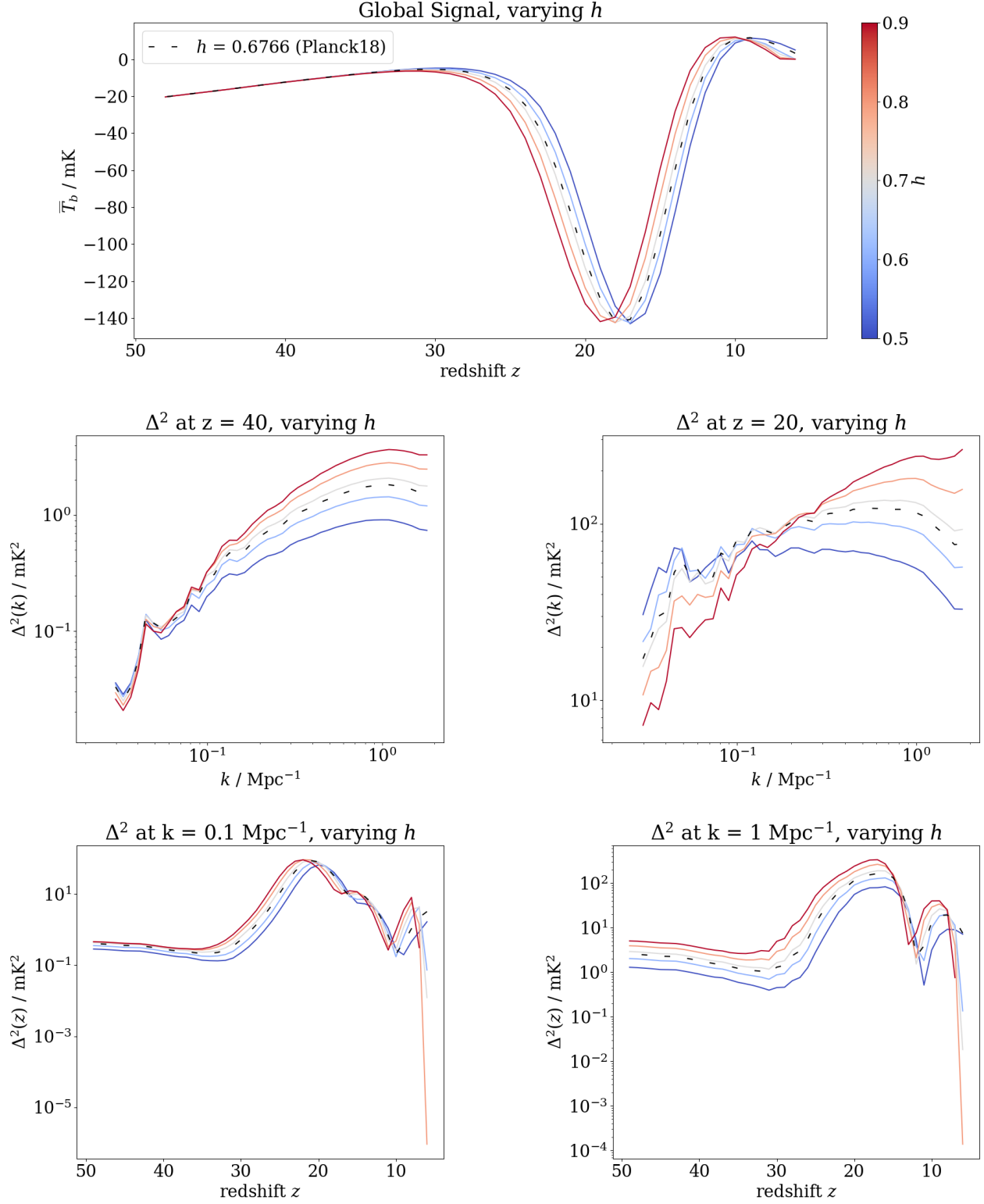
D. Varying  $h$ 

Fig. 9: For custom cosmologies varying the value of  $h$ , the 21cmSPACE simulated 21-cm global signal (top row), the simulated 21-cm matter power spectrum at fixed  $z$  (middle row:  $z = 40$  on the left and  $z = 20$  on the right), and the simulated 21-cm matter power spectrum at fixed  $k$  (bottom row:  $k = 0.1 \text{ Mpc}^{-1}$  on the left and  $k = 1 \text{ Mpc}^{-1}$  on the right). The colorbar indicates the value of  $h$  and Planck 2018 values are in black.

Changing  $h$  systematically alters the cosmic timeline by altering the relationship between cosmic time and redshift. As well as this, varying the expansion rate of the Universe changes the density of matter, even if the values of  $\Omega_m$  and  $\Omega_b$  are held constant at the conception of the universe. This imprints itself significantly onto the 21-cm global signal and 21-cm power spectra, as shown in Fig. 9, even if only taken into account through the initial conditions. In the 21-cm global signal, a higher value of  $h$  produces a shallower trough earlier in time, since increasing  $h$  means that the Universe is younger (and expanding faster) at each given redshift. Hence, there is less time for the gas to cool adiabatically relative to the CMB, and Ly $\alpha$  coupling and X-ray heating happen earlier. As a result, the gas temperature remains higher, the spin temperature is closer to  $T_{\text{CMB}}$ , and the 21-cm absorption is weaker. Although the differential brightness temperature eq: 5 does scale with  $h$ , the aforementioned effects are evidently dominant as can be seen in the top row of Fig. 9.

At  $z = 40$  the power spectrum amplitude scales modestly with  $h$  (the second row of Fig. 9), reflecting the fact that a larger Hubble constant (with fixed  $A_s$ ) gives a higher matter density and slightly enhanced growth by  $z = 40$ . Compared to low  $k$ , the effect of varying  $h$  is far more pronounced at high  $k$ : at these small scales, gas pressure is able to smooth out fluctuations, causing the turnover at  $k \sim 1 \text{ Mpc}^{-1}$ . Because higher  $h$  cases lead to hotter gas by  $z = 40$  due to denser structure, its pressure smoothing scale is larger, causing its spectrum to fall off at slightly smaller  $k$ .

At  $z = 20$ , all curves rise on large scales, then flatten or turn over close to  $k \sim 1 \text{ Mpc}^{-1}$ . On large scales ( $k \lesssim 0.1 \text{ Mpc}^{-1}$ ), the differences are less pronounced, since density contrasts are still linear. However, on small scales, the high  $h$  curves are up to an order of magnitude higher than the low  $h$  ones, with the difference stemming physically from the non-linear collapse and IGM thermal state. Since higher  $h$  has denser early structures and earlier heating, contrast on small scales is boosted. The flattening and dropping of power at highest  $k$  scales again reflect pressure smoothing of the gas: since high  $h$  models heat earlier, their gas is warmer at  $z = 20$ , increasing the Jeans scale and causing lower  $h$  curves to drop off faster than red curves.

This is consistent with the power spectra at fixed  $k$ : for both  $k = 0.1 \text{ Mpc}^{-1}$  and  $k = 1 \text{ Mpc}^{-1}$ , the earlier heating causes correlations to appear at earlier redshift, since the IGM fluctuations are larger for high  $h$ . As well as this, the spacing of the curves is more significant in the high  $k$  regime, indicating the prominence of the differences in Jeans scale.

During the interpretation of these results, it is critical to note that the lack of cosmological consistency in the 21-cm evolution is especially pertinent in the case of varied  $h$ : as  $h$  governs the behaviour of the Universe at each timestep, and in fact even plays a part in relating time to redshift coordinates, the effect of varied  $h$  in the evolution is expected to be significant. Taking these differences into account during evolution is expected to amplify differences. Therefore, the plotted results should perhaps be taken as a lower bound of possible differences, rather than the full effect of varied  $h$ .

## VI. CONCLUSIONS AND FUTURE WORK

### A. Conclusions

The dependence of initial conditions on cosmological parameters has been shown to significantly propagate through evolution during the Cosmic Dawn and EoR, imprinting differences on both the 21-cm global signal and 21-cm power spectrum.

In the case of variation of  $\Omega_m$  in cosmologies, the difference primarily manifests as a shifting of timing between astrophysical processes – higher  $\Omega_m$  cosmologies experience clumping earlier than lower  $\Omega_m$  cosmologies. This physical difference is illustrated most significantly in shifting in timing of the Cosmic Dawn absorption trough of the 21-cm global signal, with higher  $\Omega_m$  cosmologies experiencing earlier Cosmic Dawn, as well as in the 21-cm power spectrum where higher  $\Omega_m$  generally exhibits higher power across all scales and redshifts, with earlier correlations at smaller scales.

On the other hand, increasing  $\Omega_b$  appears to reduce 21-cm power spectrum amplitude at most redshifts and length scales, particularly at small scales, which could be explained by the higher baryonic pressure increasing the clumping size, smoothing out correlations at these high  $k$  modes. This is unexpected, since higher baryon density should naively increase 21-cm power; it is a possibility that the cosmological self-inconsistency during the 21-cm evolution could have a dominant effect over the initial matter power spectrum.

Finally, increasing  $h$  again affects the timing of cosmological events through its direct relationship with the ageing of the Universe. As well as this, the relationship between  $h$  and the density of the Universe is reflected in the smoothing of small-scale fluctuations during heating. Again, because of the lack of cosmological self-consistency, the results should be treated as a lower bound rather than a comprehensive picture of the full effect.

Overall, the project is a successful first step towards the implementation of variable cosmology in 21cmSPACE. While the physical results presented in this study are not yet reflective of the true physical Universe, it has been shown that the dependence of initial conditions on cosmological parameters propagates significantly through the evolution of the 21-cm signal.

### B. Future work

While initial conditions are a major factor of the 21-cm signal’s sensitivity to cosmological parameters, these parameters also enter the simulation through other dependencies as well, most notably in the halo mass function (Greig et al. 2024; Murray et al. 2013), which gives the number density of haloes at each mass. Redefinition of the halo mass function for each cosmology is essential for keeping calculations self-consistent, in order to evolve the 21-cm signal from arbitrarily early times all the way to low redshift.

After cosmology is incorporated into the evolutionary calculations, the simulation may also be extended to probe the Dark Ages. The lack of complex astrophysical processes in this era promises direct probes into fundamental cosmology. Along with proposed experiments hoping to detect the Dark Ages signal (Fialkov et al. 2024), the capability to probe this so-far poorly-understood era would provide hints into structure formation.

The existence of an independent 21-cm probe for cosmology is an invaluable tool not only for comparison with future 21-cm data, but also as a solution to problems surrounding current data analysis pipelines. For example, current parameter constraints are estimated assuming a given cosmology, which could bias the results of inference. Independence in the cosmological parameters would open up the parameter space, and allow removal of the assumptions.

Therefore, this project represents a critical foundation for the advancement of current and future cosmological probes, offering significant potential for further development.

## ACKNOWLEDGMENTS

The author thanks Prof. Anastasia Fialkov and Jiten Dhandha for thorough supervision and helpful guidance throughout the project duration.

Work done in this project also relied heavily on previously-written, public Python packages including NumPy, SciPy, Astropy, matplotlib. As well as this, numerous closed-source codes were used, including 21cmSPACE and py21cmSPACE. Some executions of these codes were performed on Cambridge University’s CSD3 and Durham University’s COSMA high performance computing clusters.

Finally, programming, research, and writing (especially in the Introduction, Cosmic History, and Design Principle sections) were significantly accelerated by generative AI tools, most notably Microsoft’s Copilot, OpenAI’s ChatGPT, and Google’s Gemini.

- 
- Ade P. A. R., et al., 2014, *Astronomy & Astrophysics*, 571, A16  
 Ade P. A. R., et al., 2016, *Astronomy & Astrophysics*, 594, A13  
 Bardeen J. M., Bond J. R., Kaiser N., Szalay A. S., 1986, *Astrophys. J.*, 304, 15  
 Barkana R., 2016, *Physics Reports*, 645, 1–59  
 Barkana R., Loeb A., 2001, *Physics Reports*, 349, 125–238  
 Beardsley A. P., et al., 2019, *Publications of the Astronomical Society of Australia*, 36  
 Brandenberger R. H., 1985, *Rev. Mod. Phys.*, 57, 1  
 Coles P., 2001, *Large-Scale Structure, Theory and Statistics* ([arXiv:astro-ph/0103017](https://arxiv.org/abs/astro-ph/0103017)), <https://arxiv.org/abs/astro-ph/0103017>  
 DeBoer D. R., et al., 2017, *Publications of the Astronomical Society of the Pacific*, 129, 045001  
 Dewdney P. E., Hall P. J., Schilizzi R. T., Lazio T. J. L. W., 2009, *IEEE Proceedings*, 97, 1482  
 Dhandha J., 2022, *First Year PhD Report*, University of Cambridge  
 Dunkley J., et al., 2009, *The Astrophysical Journal Supplement Series*, 180, 306–329  
 Eisenstein D. J., Hu W., 1998, *The Astrophysical Journal*, 496, 605–614  
 Fan X., et al., 2006, , 132, 117  
 Fialkov A., Barkana R., Tseliakhovich D., Hirata C. M., 2012, *Monthly Notices of the Royal Astronomical Society*, 424, 1335–1345  
 Fialkov A., Barkana R., Visbal E., 2014, *Nature*, 506, 197–199  
 Fialkov A., Gessey-Jones T., Dhandha J., 2024, *Philosophical Transactions of the Royal Society A: Mathematical, Physical and Engineering Sciences*, 382  
 Field G. B., 1958, *Proceedings of the IRE*, 46, 240  
 Friedrich M. M., Mellema G., Alvarez M. A., Shapiro P. R., Iliev I. T., 2011, , 413, 1353  
 Furlanetto S. R., Peng Oh S., Briggs F. H., 2006, *Physics Reports*, 433, 181–301  
 Gessey-Jones T., 2024, *PhD thesis*, Apollo - University of Cambridge Repository, doi:10.17863/CAM.110892, <https://www.repository.cam.ac.uk/handle/1810/371844>  
 Gessey-Jones T., Fialkov A., de Lera Acedo E., Handley W. J., Barkana R., 2023, *Monthly Notices of the Royal Astronomical Society*, 526, 4262–4284  
 Gessey-Jones T., Pochinda S., Bevins H. T. J., Fialkov A., Handley W. J., de Lera Acedo E., Singh S., Barkana R., 2024, *On the Constraints on Superconducting Cosmic Strings from 21-cm Cosmology* ([arXiv:2312.08828](https://arxiv.org/abs/2312.08828)), <https://arxiv.org/abs/2312.08828>  
 Greig B., Mesinger A., 2017, *Proceedings of the International Astronomical Union*, 12, 18–21  
 Greig B., Prelogović D., Mirocha J., Qin Y., Ting Y.-S., Mesinger A., 2024, *Exploring the role of the halo mass function for inferring astrophysical parameters during reionisation* ([arXiv:2403.14061](https://arxiv.org/abs/2403.14061)), <https://arxiv.org/abs/2403.14061>  
 Guth A. H., Pi S. Y., 1982, *Phys. Rev. Lett.*, 49, 1110  
 Harrison E. R., 1970, *Phys. Rev. D*, 1, 2726  
 Jeans J. H., 1902, *Philosophical Transactions of the Royal Society of London Series A*, 199, 1  
 Lewis A., Challinor A., 2007, *Physical Review D*, 76  
 Lewis A., Challinor A., 2011, *CAMB: Code for Anisotropies in the Microwave Background*, *Astrophysics Source Code Library*, record ascl:1102.026  
 Liu A., Shaw J. R., 2020, *Publications of the Astronomical Society of the Pacific*, 132, 062001

- Loeb A., Zaldarriaga M., 2004, *Physical Review Letters*, 92
- McQuinn M., Lidz A., Zahn O., Dutta S., Hernquist L., Zaldarriaga M., 2007, , 377, 1043
- Mesinger A., 2019, *The Cosmic 21-cm Revolution; Charting the first billion years of our universe*, doi:10.1088/2514-3433/ab4a73.
- Mirocha J., 2014, , 443, 1211
- Mirocha J., Furlanetto S. R., Sun G., 2017, , 464, 1365
- Murray S., Power C., Robotham A., 2013, *HMFcalc: An Online Tool for Calculating Dark Matter Halo Mass Functions* ([arXiv:1306.6721](https://arxiv.org/abs/1306.6721)), <https://arxiv.org/abs/1306.6721>
- Muñoz J. B., 2023, *Monthly Notices of the Royal Astronomical Society*, 523, 2587–2607
- Ocvirk P., et al., 2015, in *IAU General Assembly*. p. 2255292
- Planck Collaboration et al., 2014, , 571, A16
- Planck Collaboration et al., 2020, , 641, A6
- Pober J. C., et al., 2014, *The Astrophysical Journal*, 782, 66
- Pritchard J. R., Loeb A., 2012, *Reports on Progress in Physics*, 75, 086901
- Purcell E. M., Field G. B., 1956, *Astrophys. J.*, 124, 542
- Robertson B. E., Ellis R. S., Dunlop J. S., McLure R. J., Stark D. P., 2010, *Nature*, 468, 49–55
- Scott D., Rees M. J., 1990, , 247, 510
- Seager S., Sasselov D. D., Scott D., 2011, *RECFAST: Calculate the Recombination History of the Universe*, *Astrophysics Source Code Library*, record ascl:1106.026
- Semelin B., Eames E., Bolgar F., Caillat M., 2017, *Monthly Notices of the Royal Astronomical Society*, 472, 4508–4520
- Tegmark M., Zaldarriaga M., 2009, *Physical Review D*, 79
- Tseliakhovich D., Hirata C., 2010, *Physical Review D*, 82
- Visbal E., Barkana R., Fialkov A., Tseliakhovich D., Hirata C. M., 2012, *Nature (London)*, 487, 70
- Wouthuysen S. A., 1952, , 57, 31
- Zeldovich Y. B., 1972, , 160, 1P
- van Haarlem M. P., et al., 2013, , 556, A2